Glucose oxidation drives trunk neural crest cell development and fate

Nioosha Nekooie Marnany, Redouane Fodil, Sophie Féréol, Alwyn Dady, Marine Depp, Frederic Relaix, Roberto Motterlini, Roberta Foresti, Jean-Loup Duband, Sylvie Dufour

Glucose oxidation drives trunk neural crest cell development and fate

Nioosha Nekooie-Marnany[1], Redouane Fodil[1], Sophie Féréol[1], Alwyn Dady[2], Marine Depp[1]#, Frédéric Relaix[1], Roberto Motterlini[1], Roberta Foresti[1], Jean-Loup Duband[1]*, and Sylvie Dufour[1]*

[1] Univ Paris Est Creteil, INSERM, IMRB, F-94010 Creteil, France.

[2] Laboratoire Gly-CRRET, Université Paris-Est Créteil, 94000 Créteil, France

present address: Institut de Biologie, Ecole Normale Supérieure, Paris, France

* Authors for correspondence: jean-loup.duband@inserm.fr and sylvie.dufour@inserm.fr

Running title: Metabolic instruction of neural crest development

Keywords: neural crest, cell migration, fate decision, glycolysis, oxidative phosphorylation, bioenergetics

SUMMARY STATEMENT

Trunk neural crest cell migration and fate decisions rely on glucose oxidation for energy production and mobilize multiple cooperating metabolic pathways for their biosynthetic needs and execution of gene programs.

ABSTRACT

Bioenergetic metabolism is a key regulator of cellular function and signaling but how it can instruct cells' behavior and fate during embryonic development remains largely unknown. Here we investigated the role of glucose metabolism in the development of avian trunk neural crest cells (NCC), a migratory stem cell population of the vertebrate embryo. We uncovered that trunk NCC display glucose oxidation as a prominent metabolic phenotype, contrary to cranial NCC, which instead rely on aerobic glycolysis. In addition, only one pathway downstream of glucose uptake is not sufficient for trunk NCC development. Indeed, glycolysis, mitochondrial respiration and the pentose phosphate pathway are all mobilized and integrated for the coordinated execution of diverse cellular programs, epithelium-to-mesenchyme transition, adhesion, locomotion, proliferation, and differentiation, through regulation of specific gene expression. In the absence of glucose, OXPHOS pathway fueled by pyruvate failed to promote trunk NCC adaptation to environmental stiffness, stemness maintenance, and fate-decision making. These findings highlight the need for the trunk NCC to make the most of the glucose pathway potential to meet the high metabolic demands appropriate for their development.

INTRODUCTION

Cellular metabolism, long regarded as a neutral factor during development, is now recognized for its instructing role of cell fate by regulating gene networks and cell signaling (Bhattacharya et al., 2021; Miyazawa and Aulehla, 2018; Pavlova and Thompson, 2016; Shyh-Chang et al., 2013; Zhang et al., 2018). The primary function of cellular metabolism is to provide cells with bioenergetic and biosynthetic supplies from nutrients, e.g. glucose, amino-acids, and fatty acids (Zhu and Thompson, 2019). Glucose constitutes the major source for ATP production through two pathways occurring in distinct cellular compartments: glycolysis in the cytoplasm and oxidative phosphorylation (OXPHOS) in mitochondria. Glucose is also an important source of carbon for biomass production through multiple metabolic pathways branching from glycolysis. Among them, the pentose phosphate pathway (PPP) constitutes a major source of nucleotides and NADPH for anabolism (Patra and Hay, 2014).

Glucose metabolism differs among cells and depends on gene regulatory programs driving expression and activity of metabolic enzymes (Lempradl et al., 2015). Thus, in differentiated cells, it is usually catabolic with high production of ATP, as a result of entry of the glycolysis by-product pyruvate into mitochondria and OXPHOS. In contrast, in proliferating, undifferentiated cells as well as in cancer cells, glucose utilization is preferably oriented toward anabolism and ATP production relies mostly on aerobic glycolysis fed by intense glucose uptake, with extracellular lactate production and low OXPHOS activity, a process known as Warburg effect (Schell et al., 2017; Vander Heiden et al., 2009). Glucose metabolism in cells also varies in time and space to cope with environmental changes (Johnson et al., 2003; Miyazawa and Aulehla, 2018; Perestrelo et al., 2018; Shyh-Chang et al., 2013; Zhang et al., 2018). Notably, a shift from aerobic glycolysis to OXPHOS occurs in adult stem cells leaving quiescence to differentiate and in induced pluripotent stem cells exiting pluripotency (Gu et al., 2016; Ito and Suda, 2014; Perestrelo et al., 2018; Shyh-Chang et al., 2013).

Neural crest cells (NCC) constitute one of the most spectacular populations of stem cells of the vertebrate embryo (Bronner, 2018; Erickson et al., 2023; Trainor, 2013). These cells appear early all along the embryonic rostrocaudal axis in the dorsal neural tube (NT). Through epithelium-to-mesenchyme transition (EMT), NCC delaminate and disperse away from the NT to distal sites where they differentiate. Due to their partition into different populations (cranial, cardiac, vagal, trunk, and sacral) along the axis, NCC give rise to numerous cell types: skeletal and supportive tissues, endocrine cells, cardiac septum, enteric ganglia as well as peripheral neurons, glia, and melanocytes. Throughout development, NCC are exposed to different environments and cues impacting on their gene networks, cellular features, and fate (Barriga and Mayor, 2019; Chevalier et al., 2016; Duband

et al., 2015; Martik and Bronner, 2017; Soldatov et al., 2019). To date, nutrient requirements and their utilization in energy production throughout NCC development remain largely unknown. Recently, a study on avian cranial NCC delamination reported a metabolic shift toward aerobic glycolysis at onset of migration (Bhattacharya et al., 2020), suggesting that cranial NCC share metabolic properties with cancer cells. However, the other NCC populations along the embryonic axis, notably trunk NCC, differ strikingly from cranial NCC in their gene-regulatory network deployed and interaction with their environment (Li et al., 2019; Rothstein and Simoes-Costa, 2023; Scully et al., 2016; Simões-Costa and Bronner, 2015; Simões-Costa et al., 2012; Soldatov et al., 2019; Théveneau et al., 2007), and may therefore exhibit different metabolic features, possibly accounting for differences in their migratory pattern and ultimate fate.

Here, using a combination of *in vivo* and *in vitro* strategies, we investigated the role of glucose metabolism in quail trunk NCC development. We explored which metabolic pathways are recruited for their bioenergetic and biosynthetic supplies and to which extent NCC metabolic activity can drive their behavior and fate. Our results indicate that trunk NCC necessitate glucose metabolism for development and display a metabolic signature characteristic of glucose oxidation, unlike cranial NCC. We also show that though necessary, the OXPHOS pathway does not suffice for trunk NCC development, which instead involves massive mobilization of all the metabolic pathways downstream of glucose uptake, i.e. glycolysis, OXPHOS and PPP, cooperating together. Finally, our data reveal that metabolic pathways activated by nutrient inputs can drive fate decisions in NCC and raise the intriguing question that NCC metabolic activity may contribute to the identity and segregation of the different populations.

RESULTS

Glucose Metabolism is Required for Trunk NCC Development *in vivo*

To determine whether glucose metabolism is involved in trunk NCC development, we first analyzed the expression patterns of key players of glycolysis at the time of their migration (Fig. S1A), by in situ hybridization (ISH) on whole mount quail embryos and on sections. mRNAs for the glucose transporter *Glut-1*, for phosphofructokinase *PFK*, and for phosphoglycerate kinase-1 *PGK-1*, were all expressed throughout the NT at NCC pre-migratory, delamination and early migration stages (Fig. 1A). All mRNAs were evenly distributed along the NT dorsoventral axis and were also detectable in both pre-migratory and early migrating NCC (Figs. 1B, S1B). Consistently, incubation of embryos with the fluorescent glucose analog 2-NDBG as an estimate of glucose uptake revealed a staining

pattern in the NT matching that of *Glut-1* mRNA, but more pronounced at the NCC migration level (Fig. 1A).

To assess the implication of glucose metabolism in trunk NCC development, we used an *in vivo* loss-of-function strategy (Fig. S1C). 2-deoxyglucose (2-DG), a potent inhibitor of the whole glycolytic cascade (Fig. S1A), was injected *in ovo* in the caudal region of quail embryos at stages preceding onset of migration, and NCC development was subsequently followed during delamination using *Snail-2* and *Foxd-3* markers (Duband, 2010; Lukoseviciute et al., 2018; Nieto, 2002), during migration using *Sox-10* (Schock and LaBonne, 2020), and later during formation of neural derivatives using HNK-1 (Vincent and Thiery, 1984). First, qRT-PCR analyses of the caudal region 5 h post-injection revealed a robust repression of *Snail-2*, *Foxd-3* and *Sox-10* following 2-DG treatment (Fig. 1C). 2-DG also caused in a reproducible manner a delay in NCC delamination and provoked severe migration defects, ultimately resulting in aberrant patterning of the sensory and sympathetic ganglia (Figs. 1D, S2A,B). Detailed spatiotemporal analyses of migrating NCC distribution along the NT after 24 h showed that cells were either missing from the top of the NT in the caudal trunk, trapped dorsally instead of following the dermamyotome ventral side in the mid-trunk, or were absent from their target sites in the periaortic territory in the anterior trunk (Fig. 1E). Moreover, while at 10 mM 2-DG, no overt morphological perturbations of the embryo were noticed (Figs. 1D, S2A,B), at 25 mM we observed after 24 h severe defects in both the NT and paraxial mesoderm, causing ultimately tail truncation (Fig. S2A-C), as also reported previously (Oginuma et al., 2017). These results establish that *in vivo* glucose metabolism is necessary for efficient NCC dispersion and for patterning of their neural derivatives.

Glucose Metabolism is Required for Trunk NCC Dispersion in *in vitro* culture

To verify that alterations of NCC development did not merely result from indirect effects on the patterning and signaling activity of neighboring tissues and to better appreciate NCC response to glucose, we used a classical *in vitro* culture approach (Fig. S1D) in which NCC are generated from isolated trunk NT explants in defined conditions favoring delamination, migration, and differentiation with timing and kinetics comparable to those observed *in vivo* (Duband et al., 2020). First, we analyzed whether glucose is necessary for NCC dispersion and at which concentration it is the most effective, by culturing trunk NT explants in DMEM containing or not glucose and supplemented with glutamine and only 1% serum to minimize the contribution of exogenous growth factors. The behavior of the NCC population was characterized over time during delamination and migration, focusing on migratory front progression, aspect, size and cell density of the outgrowth, as well as individual cell morphology. In absence of glucose, a few NCC were capable of initiating migration,

but they rapidly failed to disperse away over time and showed a poorly-spread morphology and low density (Figs. 1F-H, S3A,B). In the presence of glucose, in contrast, NT rapidly produced large and dense NCC outgrowths expanding fast during the first 24 h and with numerous well-spread cells (Figs. 1F-H, S3A,B), as observed in classical serum-rich media (Dupin et al., 2018; Rovasio et al., 1983; Santiago and Erickson, 2002). Glucose favored NCC spreading at all concentrations tested, but maximal NCC outward progression, with robust and sustained individual cell velocity, high persistence and density, was reached at 5 mM (Fig. S3C-G), which was the concentration used for the rest of the study.

Because pyruvate provided as a nutrient can be an alternative entry point to fuel OXPHOS independently of glucose (Fig. S1A), we compared its ability to support NCC development to that of glucose. In pyruvate, NCC dispersion occurred almost normally at culture onset, but it decreased strongly after 5-8 h, with cells exhibiting elongated spindle-shaped morphologies (Figs. 1F, S3A). Pyruvate was systematically less efficient than glucose to promote NCC dispersion, with significantly reduced NCC outgrowths, cell densities and outward progressions at all concentrations tested (Figs. 1F-H, S3A-D). Maximal NCC dispersion and individual cell velocity were reached at 1-2 mM while persistence was greater for concentrations ≥ 2 mM (Fig. S3E,G). Furthermore, pyruvate did not support NCC spreading over time at 0.1 mM while it induced extensive NCC flattening at high concentrations (Fig. S3C). Therefore, throughout the study, pyruvate was used at 1 mM.

To identify possible additive or cooperating effects of glucose and pyruvate, we analyzed responses of NT explants to both compounds used in combination. We found that NCC outgrowth aspect, progression, and cell morphologies were virtually indistinguishable from those observed in glucose alone (Figs. 1F-H; S3B), thereby establishing the predominant role of glucose in supporting NCC development. Lastly, we analyzed the effect of 2-DG on NCC dispersion in culture. In its presence, NCC initially segregated normally from the NT, and their outgrowth area and progression were close to those of untreated explants (Fig. 1F,G), but cells were less dense, with a spindle shape, as observed in pyruvate condition. Then, expansion of the population stalled almost completely (Fig. 1H), and NCC started to round up, resulting in sparse cells occupying a limited area around the NT (Figs. 1F,G, S5A,B).

Finally, we investigated the expression of the glucose transporter Glut-1 and glycolytic enzymes in NCC in culture. Glut-1 was expressed similarly on the surface of NCC in glucose or in pyruvate (Fig. S1E), consistent with their capacity to adsorb glucose under both conditions, as judged on 2-NDBG uptake (Fig. S1E). *Glut-1* and *PFK* mRNAs were low in NCC and more strongly expressed in the NT (Fig. S1F), and they were both up-regulated in the presence of glucose compared

to pyruvate (Fig. S1F,G). In contrast, *PGK-1* was strongly expressed in both the NT and migrating NCC and was not affected by nutrient supplies (Fig. S1F).

Together, these results show that like *in vivo*, trunk NCC cultured *in vitro* can metabolize glucose using the glycolytic machinery and that glucose metabolism is necessary for their efficient dispersion. Moreover, pyruvate, a by-product of glycolysis, cannot be substituted for glucose for efficient migration.

Trunk NCC display a Typical OXPHOS Signature during Dispersion

To identify the metabolic pathways downstream to glucose uptake that are involved in trunk NCC dispersion *in vitro*, we performed metabolic profiling of NT explants by measuring mitochondrial respiration and glycolysis using a Seahorse XF analyzer and by quantifying the amount of ATP produced and lactate released at the end of the Seahorse assay (Fig. 2). Analyses of the bioenergetic profiles of individual explants exposed to glucose, pyruvate, or a combination of both, associated with MitoStress assays, revealed that in all conditions a great majority of the explants display at initiation of migration at 5 h an OXPHOS signature characterized by high oxygen consumption rate (OCR) and low extracellular acidification rate (ECAR) (Fig. 2A,B). In addition, no change in metabolic activity was observed after 24 h (Fig. 2B). As previously reported for chick cranial NCC (Bhattacharya et al., 2020), quail cranial NT explants at 5 h exhibited a typical aerobic glycolysis profile characterized by a lower OCR and a high ECAR (Fig. 2B). Interestingly, in glucose, greater values of OCR and ECAR (Fig.2A,D) and ATP production (Fig. 2F) were observed than in pyruvate. These results indicate that, unlike in cranial NCC, glucose is mobilized in trunk NCC to feed the mitochondrial OXPHOS pathway rather than for lactate production, and that a better yield in energy production is obtained for glycolysis coupled to OXPHOS than for OXPHOS fueled by pyruvate alone.

Then, we evaluated the impact of metabolic inhibitors (Fig. S1A) on the bioenergetic activity of trunk NT explants. 2-DG caused a sharp drop in OCR with no alteration in ECAR, shifting the metabolic profile toward metabolic quiescence (Fig. 2C-E). A similar result was obtained with oligomycin, an inhibitor of mitochondrial ATP synthase (Fig. 2C-E). Moreover, both 2-DG and oligomycin decreased OCR levels (Fig. 2E) and sharply reduced ATP production (Fig. 2F), but did not affect extracellular lactate production (Fig. 2G). Of interest, inhibitor effects were similar in all nutrient conditions, but in medium containing glucose and pyruvate, 2-DG reduced ATP production to the same levels as in glucose alone (Fig. 2F), suggesting that pyruvate could not efficiently compensate for glycolysis inhibition.

These results demonstrate that, in trunk NT explants in culture, most of the ATP production relies primarily on glucose oxidation through OXPHOS, and reveal that OXPHOS inhibition does not cause metabolic rewiring to aerobic glycolysis, as observed previously in cranial NCC (Bhattacharya et al., 2020), pointing to possible different metabolic regulatory processes in distinct NCC subpopulations.

OXPHOS Plays a Critical Role in Trunk NCC Development

We next tested whether the OXPHOS pathway is required for trunk NCC development. Similarly to 2-DG, *in ovo* injection of oligomycin at 1 μM caused a significant decrease in *Snail-2*, *Foxd-3* and *Sox-10* expressions (Fig. 3A) and a severe reduction in *Foxd-3* expression in the dorsal NT at delamination after 5 h, then a massive decrease in the number of *Sox-10*+ cells during migration after 24 h, and lastly a complete disruption of the sensory and sympathetic ganglia after 48 h (Figs. 3B,C, S4A-C). Moreover, at 5 μM oligomycin, patterning of the NT and paraxial mesoderm was strongly disrupted after 24 h, resulting in complete absence of the lower trunk (Fig. S4A-C).

When applied onto NT explants in culture, oligomycin affected initial NCC progression, with cohesive cells and reduced outgrowth area (Figs. 3D,E, S5A). Then, NCC expansion decreased strongly, producing a small outgrowth of sparse, poorly-spread cells at 24 h (Figs. 3D,E, S5A,B). We also tested the effect of other OXPHOS inhibitors, such as rotenone combined with antimycin-A (Rot.-AA) as well as an inhibitor of the mitochondrial pyruvate carrier UK-5099 (Fig. 1A). Both Rot.-AA and UK5099 had a similar effect to oligomycin except that reduction in dispersion was more immediate and massive with Rot.-AA (Figs. 3D-F, S5A,B). Oligomycin also exerted a much stronger effect on NCC cultured in pyruvate than in glucose, with abrogated cell dispersion (Fig. S5C). Likewise, UK-5099 affected severely NCC dispersion and spreading in pyruvate and more moderately in glucose (Fig. S5C). Finally, we verified that, consistent with their aerobic glycolytic profile, cranial NCC dispersion in culture is strongly affected by 2-DG and only weakly by oligomycin (Fig. S5D), as also shown in chick (Bhattacharya et al., 2020). These results establish that active OXPHOS is required for trunk NCC development and more dispensable in cranial NCC, further illustrating the metabolic specificities of each population.

PPP is Mobilized during Trunk NCC Dispersion

Rapid and sustained expansion of trunk NCC cells requires most likely an intense biosynthetic activity beside high bioenergetic needs. We therefore investigated whether NCC development also relies on PPP using 6-aminonicotinamide (6-AN), a blocker of PPP. In culture, 6-AN showed no

apparent effect on the initial dispersion of NCC, but the progression of cells slowed down after 5-8h, and a strongly reduced outgrowth with many round cells was observed (Figs. 3D-F, S5A,B). 6-AN greatly affected NCC dispersion in glucose but had little effect in pyruvate (Fig. S5C). Moreover, in Seahorse analyses, 6-AN had no effect on OCR and ATP levels (Fig. 2C-F), suggesting a minor contribution of PPP to energy production. When applied *in vivo*, 6-AN did not show much effect on NCC delamination, as judged on the *Foxd-3* expression pattern, but it inhibited markedly NCC migration after 24 h, similarly to 2-DG and oligomycin (Fig. S4B,D). These results thus show that beside glucose oxidation, PPP contributes to trunk NCC development, thereby suggesting the involvement of multiple metabolic pathways possibly acting in a cooperative manner to support coordination between multiple cellular processes: EMT during delamination, changes of substratum and cell adhesion, activation of the locomotion machinery, and proliferation.

Glucose Oxidation is Required for EMT during Trunk NCC Delamination

For delamination, we evaluated first the NT capacity to produce NCC over time in 20 h-culture under different nutrients and in the presence of metabolic inhibitors. We found that the duration of NCC production was significantly shorter with pyruvate than glucose and considerably reduced by all inhibitors (Fig. 4A). Next, we developed an assay suitable for discriminating delaminated from migrating NCC on 5 h explants (Fig. 4B). We observed that the number of delaminated NCC was much higher in glucose and glucose supplemented with pyruvate than in pyruvate alone and was halved in 2-DG, oligomycin, or Rot.-AA, but not by 6-AN (Fig. 4C). Immunolabeling showed that Snail-2, a major EMT player (Duband, 2010; Nieto, 2002), high in delaminated NCC and declining gradually in migrating cells in glucose-containing medium, was strongly diminished in both NCC compartments in explants cultured in pyruvate or with 2-DG (Fig. 4D,E). In contrast, consistent with an unchanged delamination rate in response to 6-AN (Fig. 4C), NCC displayed similar Snail-2 staining under PPP inhibition (Fig. 4D,E). Intriguingly, with OXPHOS inhibitors and particularly with Rot.-AA, Snail-2 completely disappeared in delaminated NCC but remained high in migrating ones (Fig. 4D,E). Expression of *Snail-2* mRNA was strongly diminished in pyruvate or with 2-DG and halved by oligomycin (Fig. 4F,G), consistent with the reduction of Snail-2 protein. Conversely, *Snail-2* expression was not much altered by Rot.-AA (Fig. F,G), probably as a result of its increase in the migrating pool. Together, these data indicate that glucose oxidation is required for NCC delamination and *Snail*-2 expression. In addition, PPP is dispensable for delamination but is necessary for long-term production of NCC, as indicated by the experiments using pyruvate alone or 6-AN.

Multiple Metabolic Pathways Cooperate for Trunk NCC Locomotion

We next investigated the contribution of glucose metabolism to trunk NCC locomotion in culture using video-microscopy analyses. In glucose condition, NCC generally exhibited high velocity and persistence over 18 h, leading to linear trajectories oriented perpendicular to the NT (Figs. 5A, S6A,B), while in pyruvate, velocity and persistence decreased gradually, leading to shorter trajectories (Figs. 5A, S6A,B). In absence of both glucose and pyruvate, NCC migration tracks were very short, resulting from low velocity associated with fair persistence (Figs. 5A, S6A,B), while in both nutrients, NCC displayed high and sustained velocity and persistence over time and long trajectories as in glucose alone. With 2-DG, cells trajectories were at first relatively linear but became more random with time (Fig. S6C), the most striking effect being a rapid and continuous decrease of velocity over time resulting in migration arrest (Fig. 5B). Cell trajectories were generally not much affected by oligomycin (Fig. S6C), while velocity was decreased during the first 6 h. Subsequently NCC migration became extremely random with decreased persistence and higher velocity (Fig. 5B). Interestingly, Rot.-AA showed a much stronger effect than oligomycin. Trajectories were very short because velocity was almost knocked-out immediately after addition and remained weak during 8 h (Figs. 5B, S6C), but as with oligomycin, velocity increased progressively with time and persistence decreased. In UK-5099, cells trajectories were more random, associated with low persistence (Figs. 5B, S6C). Lastly, 6-AN affected velocity strongly and gradually at least during the first 8 h (Figs. 5B, S6C). These results therefore illustrate the critical contribution of glucose oxidation to NCC locomotion and also reveal that this process relies on additional metabolic processes, notably PPP.

Glucose Metabolism Coordinates Trunk NCC Substrate and Cell Adhesions

To gain insight into the role of glucose metabolism on trunk NCC adhesion in culture, we examined by immunolabeling the cellular localization of paxillin and β-catenin, two cytoplasmic partners of integrins- and cadherins-adhesion complexes, respectively. NCC developed substrate adhesions in all conditions at 5 h but they were reduced in absence of glucose and pyruvate (Fig. 5C,D). At 24 h, their number increased with glucose while it remained stable in pyruvate or in the absence of nutrients (Fig. 5D). In addition, the number of substrate adhesions was significantly reduced with 2-DG and increased with oligomycin, consistent with changes in cell spreading (Fig. 5C,D). Substrate adhesions differed also in their shape and area with the nutrient conditions: they were larger and more elongated in pyruvate compared to the other conditions (Fig. S6E). Finally, NCC were always engaged in cell-cell contacts with their neighbors in medium containing glucose while in pyruvate, they remained mostly as individuals (Fig. S6F). The number of cell-cell adhesions at 5 h was increased substantially with oligomycin and Rot-AA (Fig. S6G, H). These data indicate that the balance between substrate and cell-cell adhesion in trunk NCC is influenced by glucose metabolism.

Trunk NCC Mechanics and Response to External Stiffness are Modulated by Nutrient Inputs

NCC are able to sense the extracellular matrix rigidity in their environment, which in turn modulates their adhesion and migration capacity (Barriga et al., 2018; Chevalier et al., 2016; Marchant et al., 2022; Shellard and Mayor, 2021). To determine whether mechanotransduction activities in trunk NCC are under metabolic control, we investigated the impact of nutrients on their adhesive and migratory response in culture to fibronectin-coated polyacrylamide gels with different stiffness in the range of avian tissue rigidity at early embryonic stages, from soft (1.2 kPa) to stiff (6.3 kPa) (Chevalier et al., 2016). As on glass (Fig. 5C), NCC on stiff and soft gels developed substrate adhesions irrespective of the nutrient supplied (Fig. S6I). Moreover, we found important discrepancies in NCC response to gel rigidity with the nutrients (Fig. 5E-G). In glucose, the number of substrate adhesions (Fig. 5E) and the progression of the population were not significantly different between stiff and soft gels, while velocity and persistence were only slightly lower on soft gels (Fig. 5F,G). In contrast, on soft gels, in medium containing pyruvate or both nutrients, NCC displayed less substrate adhesions and their velocity and the progression of the population were significantly lower (Fig. 5E-G).

We then studied NCC stiffness and traction activity on the gel using atomic force and traction force microscopy (Fig. 5H-J). Measurement of cellular stiffness revealed that with glucose, NCC adapted their stiffness to that of the substrate in both soft and stiff gels, whereas in pyruvate they failed to increase their stiffness to the level of the stiff gel (Fig. 5H). NCC traction activity in soft and stiff gels (expressed as stress/cell) was constant in glucose whereas in the presence of pyruvate, it was higher in stiff gels (Fig. 5I,J). By calculating the product of the average distance covered per h and the average force (stress/cell/area) we estimated the energy produced when NCC moved on the gels under the different nutrient conditions (Table I). Energy produced was similar in all nutrients on stiff gels, while it was lower on soft gels in pyruvate compared to glucose in which it was almost unchanged.

These data indicate that trunk NCC are mechanoresponsive as described previously for cranial and enteric NCC (Barriga et al., 2018; Chevalier et al., 2016; Marchant et al., 2022; Shellard and Mayor, 2021), but also that their response is determined by specific metabolic activities. In glucose, owing to their capacity to accommodate their stiffness and energy production to their environment, NCC are endowed with the ability to migrate under diverse biophysical constraints. In pyruvate, NCC are less prone to modulate their stiffness and negatively respond to modifications in the rigidity of their environment by decreasing their adhesive and migratory response.

Multiple Metabolic Pathways are Required for Cell Cycle progression and proliferation of Trunk NCC

Contrary to many motile cells, NCC maintain active cell division throughout migration, and this process contributes strongly to expansion of the population (Ridenour et al., 2014). On the other hand, cell cycle progression from G1-S phase is required for delamination (Burstyn-Cohen and Kalcheim, 2002). We then analyzed the influence of glucose metabolism on trunk NCC cycling and proliferating activity in culture using EdU incorporation. During delamination, numerous EdU+ NCC could be identified along the NT apical side (Fig. S7A), and addition of glycolysis or OXPHOS inhibitors dramatically reduced their numbers (Fig. S7A). During migration, while EdU incorporation was weak at 5 h and minimal after 24 h in absence of glucose and pyruvate (Fig. S7B), it remained very intense over time in glucose alone and in glucose and pyruvate (Fig. 7B). In pyruvate alone, in contrast, EdU incorporation was strong at initial migration but was dramatically reduced after 24 h (Fig. S7B). All metabolic inhibitors decreased both the EdU-staining intensity and the proportion of EdU^+ NCC at both 5 h and 24 h (Fig. S7C). These data indicate that multiple metabolic pathways are implicated in a cooperative manner in the control of cell cycling and proliferation of trunk NCC.

Glucose and Pyruvate Differently Influence Trunk NCC Pluripotency and Differentiation Potential

To investigate whether metabolic activity affects NCC stem cell capacity and influences their differentiation potential, we analyzed in culture the expression patterns of the transcription factors Sox-10 and Foxd-3, which have been shown to be essential regulators of NCC pluripotency beside their role in delamination and migration (Lukoseviciute et al., 2018; Schock and LaBonne, 2020; Simões-Costa et al., 2012). At 5 h (Fig. 6A,B,E), levels of Sox-10 protein and *Sox-10* and *Foxd-3* mRNAs were much reduced in delaminating and migrating NCC cultured with pyruvate, compared with those cultured with glucose in which the vast majority of migrating NCC exhibited Sox-10+ nuclei. 2-DG strongly diminished the number of Sox-10+ cells, while oligomycin and Rot.-AA caused an overall reduction of Sox-10 intensity in all NCC (Fig. 6C). Likewise, *Sox-10* and *Foxd-3* mRNA levels dropped strongly with 2-DG (Fig. 6D), as also observed *in vivo* (Fig. 1C-E), while those for *Sox-10* showed a trend toward a reduced expression that failed statistical testing with oligomycin and Rot-AA. In addition, *Foxd-3* expression was selectively repressed by 2-DG, oligomycin or Rot.-AA in pre-migratory NCC but less so in delaminating and migrating cells (Fig. 6E). At 24 h, repression of *Sox-10* and *Foxd-3* expression was even more pronounced in absence of glucose or in the presence of metabolic inhibitors, including 6-AN (Fig. S8A,B).

We next evaluated the influence of glucose metabolism on the trunk NCC capacity to differentiate in culture. After 3 days, several populations of cells were identified: Sox-10+ and HNK-1+ NCC progenitors characterized by their stellate shape, Tuj-1+ neurons displaying long cell processes, as well as other cells presenting a great diversity of morphologies, including MITF+ melanoblasts and large, flattened α-SMA+ myofibroblasts (Fig. S8C). In glucose-containing medium, the proportion of NCC progenitors remained high over time while the number of neurons and melanoblasts increased up to 20% and 30-40%, respectively (Fig. 6F). In contrast, in pyruvate medium, the proportion of NCC progenitors dropped to less than 50% with time at the benefit of myofibroblasts, reaching 40% of the population (Fig. 6F). Of note, the number of melanoblasts did not increase much in pyruvate medium while the number of HNK1+ cells was constantly very low (Fig. 6F). A likely explanation for this persistent absence of HNK-1 staining is that the HNK-1 epitope is a glycoconjugate moiety needing glucose for its biosynthesis (Tucker et al., 1984).

These results indicate that glucose metabolism is required for maintenance of high levels of pluripotency markers during NCC migration and that NCC differentiation programs are influenced by nutrient inputs, with glucose favoring neural and melanoblast differentiation, while pyruvate promotes a limited range of phenotypes where myofibroblasts are predominant.

DISCUSSION

Our study illustrates the critical role of glucose metabolism in quail NCC development. We report that glucose is required both *in vivo* and in *in vitro* culture for quail trunk NCC dispersion. In addition, trunk NCC display a typical OXPHOS signature, and glucose oxidation through glycolysis coupled to OXPHOS plays a critical role in their dispersion. Blockers of glycolysis and OXPHOS affected every aspect of NCC development associated with a sharp drop in mitochondrial respiration and ATP production. Additionally, our data establish that OXPHOS is not sufficient to support all the cellular events involved in this process as systematic inhibition of glycolysis compromised NCC dispersion, even in the presence of pyruvate to support OXPHOS. Likewise, a PPP inhibitor strongly affected NCC dispersion despite a minimal effect on mitochondrial respiration and ATP production. Finally, pyruvate alone failed to support complete dispersion, division, and differentiation of NCC, while glucose could elicit the complete cellular response of NCC, i.e. delamination, adhesion, migration, proliferation, maintenance of stemness, and widespread differentiation. Glucose also potentiates NCC stiffness adaptation to that of their microenvironment and supports optimal dispersion, illustrating the prominent role of glucose metabolism in NCC adaptation to physical changes in the environment.

Thus, contrary to the general assertion that OXPHOS has a bioenergetic role in differentiated cells and that aerobic glycolysis has a biosynthetic role in proliferating non-differentiated stem cells (Ito and Suda, 2014; Shyh-Chang et al., 2013), trunk NCC development relies on the concerted and sustained mobilization of all metabolic pathways dependent on glucose metabolism, i.e. glycolysis, OXPHOS, and PPP, cooperating together (see model, Fig. 7). These findings illustrate the necessity for the NCC population to make the most of the potential of the carbon metabolism route, so that they are endowed with the capacity to meet the metabolic demands required for the coordinated execution of diverse cellular events. How NCC maintain balanced activities of the different metabolic pathways is currently unknown. This may be achieved through regulated levels of metabolic enzymes and products of each pathway, under the control of intrinsic genetic programs as well as extrinsic factors, including nutrient availability and demand (Lempradl et al., 2015). This view is supported by our observations as well as a recent report (Oginuma et al., 2017) that glycolytic enzymes are not uniformly expressed in the embryo at the time of NCC dispersion.

Our data reveal that trunk NCC display metabolic requirements and features toward glucose distinct from their cranial counterparts. Indeed, quail cranial NCC display a Warburg effect similarly to chick cranial NCC (Bhattacharya et al., 2020). Thus, although trunk and cranial NCC possess in common a number of cellular and molecular features, such as signaling pathways, EMT, and migration properties, they do not share the same metabolic status. This reflects the strong adaptability of NCC to a great variety of environmental conditions throughout development, at the origin of the diversity in their migratory behaviors and fates. Indeed, difference in metabolic activity between cranial and trunk NCC can also reside in the local O_2 concentration in their environment. As for cancer cells in which hypoxia is known to promote metastatic spread (Semenza, 2012), cranial NCC reside in a hypoxic milieu, and exposure to high O_2 levels or knockdown of the hypoxia-inducible factor HIF-1 cause attenuation of their production associated with strong reduction of *Snail-2* expression (Scully et al., 2016). Trunk NCC dispersion in contrast is intimately associated with blood vasculature (Schwarz et al., 2009; Thiery et al., 1982), and it is not affected by high O_2 levels or by deletion of the HIF-1 gene (Iyer et al., 1998; Morriss and New, 1979).

We could not attribute to any metabolic pathway a specific role in the basic cellular processes, adhesion, locomotion and division. For example, despite PPP having a well-recognized role in nucleotide synthesis and maintenance of cellular redox balance (Patra and Hay, 2014), this pathway was not recruited solely for NCC proliferation but significantly contributed to cell velocity and persistence of movement as well. Likewise, OXPHOS and ATP production in mitochondria were not exclusively aimed at supporting active migration, but also played a key role in EMT and proliferation. A likely explanation is that these processes are extremely demanding in both bioenergetic and

biosynthetic supplies (Salazar-Roa and Malumbres, 2017; Zanotelli et al., 2021). Another reason is that enzymes, metabolites and byproducts of metabolic pathways are known to influence cellular programs independently of their canonical bioenergetics and biosynthetic roles (Miyazawa and Aulehla, 2018). For example, NADH produced through TCA protects cells from oxidative stress (Bigarella et al., 2014; Khacho et al., 2016). Likewise, similarly to neurons (Herrero-Mendez et al., 2009), the use of the PPP for metabolizing glucose may ensure NADPH production for the maintenance of a cellular redox balance. TCA cycle intermediates, in particular acetyl-CoA and α-ketoglutarate, are involved in epigenetic regulation through histone acetylation and methylation (Kaelin and McKnight, 2013). Regulation of gene expression during NCC formation is under tight epigenetic control, involving DNA methylation, histone modifications, and ATP-dependent chromatin remodelers (Hu et al., 2014). Our finding of alterations of developmental programs such as delamination and maintenance of stemness upon manipulating nutrient availability and metabolic pathways in NCC is therefore in favor of a direct role of cellular metabolism in regulation of nuclear transcription programs in NCC through epigenetic regulation (Boon et al., 2020; Traxler et al., 2021; Tsogtbaatar et al., 2020).

In conclusion, our data show that NCC in the embryonic trunk region rely primarily on glucose oxidation through glycolysis and mitochondrial respiration for energy production and mobilize a large range of metabolic pathways downstream to glucose uptake to meet their bioenergetics and biosynthetic needs as well as to instruct their gene circuits driving their behavior and fate. These findings therefore reveal the intricate integration of cellular metabolism to basic cellular processes underlying cell behavior. How these metabolic pathways are regulated to accommodate the different steps of NCC formation both temporally and spatially remains to be investigated.

MATERIALS AND METHODS

Reagents

Bovine plasma fibronectin (1 mg/ml stock) was from Sigma (cat. no. F1141). Dispase II at 5 U/ml stock solution in Hanks' balanced saline was from Stemcell Technologies (cat. no. 07913). The following chemicals were prepared and used according to the manufacturers' guidelines: 2-deoxy-D-glucose (2-DG, Sigma, cat. no. D8375), oligomycin-A (Sigma, cat. no. 75351), rotenone (Sigma, cat. no. R8875), antimycin-A (Sigma, cat. no. A8674), FCCP (Sigma, cat. no. C2920), 6-aminonicotinamide (6-AN, Cayman Chemicals, cat. no. 10009315), and UK-5099 (Tocris Biosciences, cat. no. 4186). 2-DG was prepared as a 1 M stock solution in glucose-, pyruvate- and

glutamine-free DMEM and used at 5-10 mM for *in vitro* experiments and at 10-25 mM for *in ovo* injections; oligomycin, rotenone-antimycin-A (Rot.-AA), and FCCP were prepared in the vehicle DMSO at 10 mM, diluted as stock solution in culture medium at 100 μM, and used at 1 μM for *in vitro* experiments and at 1-5 μM for *in ovo* injections; UK-5099 was prepared as 100 mM solution in DMSO and used at 100 μM; and 6-AN was prepared as 100 mM solution in DMSO and used at 100 μM for *in vitro* and *in vivo* experiments, and at 500 μM in Seahorse analyses. As we previously showed that 1/1000 dilution of DMSO has not effect on NCC behavior (Monier-Gavelle and Duband, 1995), in experiments using this dilution, the corresponding controls were performed without addition of DMSO. When DMSO dilution was below 1/1000, the same dilution of DMSO but without the drug was used for controls.

Embryos

Quail embryos were used throughout the study. Fertilized quail eggs were purchased from a local farm (La Caille de Chanteloup, Corps Nuds, France). Eggs were incubated at 37-38°C for until embryos reached the desired developmental stages. Embryos were staged using the Hamburger and Hamilton (HH) chart (Hamburger and Hamilton, 1951) and based on the number of somite pairs.

***In ovo* injection of drugs**

I*n vivo* loss-of-function experiments were performed on embryos at stage HH12-13 (15-16 somite pairs). After removing of 1 ml of albumin from the egg and opening of the shell with curved dissecting scissors to expose the embryo to the experimenter, the drugs were injected at the tip of the tail bud of the embryo into the lumen of the NT and under the vitelline membrane in the vicinity of the NT over the unsegmented region and the last 3-5 somites (10 µl delivered per injection). For controls embryos were injected with the vehicle only. The eggs were sealed with tape and were further incubated at 38°C in a moist atmosphere for 5-48 h. Monitoring of NCC development was performed by following expression of marker genes by whole mount in situ hybridization at 5, 24 and 48 hours followed by sectioning and qRT-PCR at 5 h (see below).

Cell Culture

Generation of NCC primary cultures: Trunk and cranial NCC cultures were produced from NT explants obtained from quail embryos at stages HH 13-15 (19-25 somite pairs) and at stages HH 8-9 (5-8 somite pairs), respectively (Duband et al., 2020). After opening of the eggshell, the yolk was transferred into phosphate-buffered saline (PBS). The embryo was cut off from the yolk and

transferred into PBS in an elastomer-containing dish. An embryo portion of about 750-μm long was excised at the level of the last 5 somites for trunk NCC and of the whole cranial region up to the first somite for cranial NCC with a scalpel under a stereomicroscope and subjected to mild enzymatic digestion by treatment with dispase II at 2.5 U/ml for 5-10 minutes at room temperature. The NT was dissected out manually using fine dissection pins under a stereomicroscope, freed from the surrounding tissues, and transferred for 30-60 minutes in DMEM medium (w/o. glucose, w/o. pyruvate, Gibco, cat. no. 11966025) supplemented with 0.5% fetal bovine serum for recovery from enzyme treatment. NT were explanted onto culture dishes or glass coverslip previously coated with fibronectin at 10 μg/ml in PBS (i.e. about 5 μg/cm^2) for a minimum of 1 h at 37°C. To ensure rapid initiation of NCC migration, NT were positioned with their dorsal side oriented down toward the substratum. Explants were cultured at 37°C under normoxic conditions in a humidified 5%-CO_2 incubator in DMEM containing 1% serum, 100 U/ml penicillin, 100 µg/ml streptomycin, 2 mM glutamine, and supplemented with 5 mM glucose and 1 mM pyruvate. In some specified cases, glucose was used at 0.1-25 mM and pyruvate at 0.1-5 mM. The choices of the culture dish, culture medium, and duration of the culture were determined according to the purpose of the experiment and the method of analysis used (see below). Throughout each experiment, the morphology of the NT explant, area and progression of the NCC outgrowth were evaluated, imaged, and assessed regularly under an inverted phase contrast Nikon microscope equipped with 6.3X, 10X, and 20X objectives.

Quantification of outgrowth area and density: To measure the NCC outgrowth area and NCC density, phase contrast images of explants encompassing half of the NCC outgrowth with the NT situated along the long axis of the image were taken with the 10x objective. The size of the image corresponded to a rectangle about 400 μm wide and 600 μm long. The area occupied by NCC in the whole image and defined as surface occupancy in pixel^2 was measured using ImageJ while NCC density defined as number of cells per field was calculated by counting the total number of cells in a square of 200 μm on each side.

Delamination assay: NT explants were cultured for 5 h, a time sufficient to allow NCC segregating from the dorsal NT to adhere to the substrate. NT was then removed manually from the dish using fine dissection pins under a stereomicroscope or by gentle flushing of culture medium with a pipet tip, to uncover delaminated cells. Delaminating cells were discriminated from migratory cells by several criteria: their strong Snail-2 content, their central position in the outgrowth often separated from the migration zone by a cell-free gap, their reduced size, and their compact shape. The numbers

of delaminated and migrating cells were measured using images taken with a 10X objective and encompassing the mid-part of the explant along its long axis. Cells were counted in a rectangle 100-µm wide and 250-µm long covering the areas of delaminated cells or of migrating cells using ImageJ.

Cellular Bioenergetic Analyses

OCR and ECAR measurements: Bioenergetic profiles of NCC primary cultures were determined using a Seahorse Bioscience XF24 Analyzer. A single NT explant was deposited precisely at the center of each well of 24-well Seahorse plate previously coated with fibronectin in culture medium at 37°C in a humidified 5%-CO_2 incubator, and NCC were allowed to undergo migration for 1.5 h or overnight depending to the purpose of the experiment. Before preparation of the plate for Seahorse analysis, the areas of the NT explants were measured for normalization. Cultures were then rinsed in Seahorse XF medium (Agilent, cat. no 103575-100) without serum and incubated for 1 h at 37°C in normal atmosphere. Then, the Seahorse assay was run according to the manufacturer's instructions. Oxygen consumption rate (OCR) and extracellular acidification rate (ECAR) values, as readouts of basal mitochondrial respiration and glycolysis respectively, were assessed regularly every cycle (mix, wait and measurement during 3 minutes), the basal measurement consisting of 4 cycles and drug injections, 3 cycles during 30 minutes. The key parameters of mitochondrial respiration (ATP-linked respiration, maximal respiratory capacity and proton leak) were measured by means of a MitoStress test after sequential additions of oligomycin (1 μM), FCCP (0.75 μM), and Rot.-AA (1 μM) through 3 cycles of measurements in 30 minutes. When appropriate, NCC primary cultures were processed after Seahorse analysis for intracellular ATP level and lactate measurement.

Seahorse Agilent assay defined energetic maps for cell metabolic phenotypes comprised of four quadrants: quiescent, aerobic (OXPHOS), glycolytic, and energetic. We designed an adaptation of Agilent energetic map to our system by assessing OCR and ECAR in NT explants under starvation medium, i.e. in DMEM with 2 mM glutamine without glucose and pyruvate, and in conditions with 5 mM glucose and 1 mM pyruvate. Basal respiration measured was between 120-200 pmole/min. under the starvation condition and 300-400 pmole/min. in the presence of nutrients, respectively. This difference between the levels of OCR in these two conditions allowed us to fix the OCR threshold between the quiescent and OXPHOS quadrant at 200 pmole/min. The ECAR threshold between the quiescent and glycolytic quadrants was set at 30 mpH/min. to achieve an OCR/ECAR ratio of 4, using as references previous studies which established that glycolysis was the major contributor to ECAR for baseline cellular OCR/ECAR ratio < 4 (Konrad et al., 2017; Mercier-Letondal et al., 2021). Data shown in our energetic maps correspond to the mean OCR and ECAR values ± s.d. of the fourth measurement of basal respiration and of the third measurement after inhibitor treatment.

ATP and lactate measurements: Intracellular ATP and extracellular lactate levels were measured for each NCC primary cultures after Seahorse analysis using an ATPlite Bioluminescence assay kit from PerkinElmer (cat. no. 6016943) and the Lactate Fluorometric Assay kit from BioVision (cat. no. K607), respectively, according to the manufacturers' instructions.

mRNA Quantification by Quantitative RT-PCR

For cell cultures, total RNA of cells from 5-8 NT explants were extracted using the Ambion PureLink RNA Mini Kit (Invitrogen, cat. no. 12183018A) following the manufacturer's guidelines. For injected embryos, the NT situated in the caudal part encompassing the last 5 somites up to the tail bud was dissected manually with fine dissection pins, and the total RNA was extracted using Trizol (Invitrogen) according to manufacturer instructions. After quantification of RNA concentration, 500 ng RNA were used for cDNA synthesis using SuperScript IV reverse transcriptase (Invitrogen, cat. no. 18090050). Quantitative real time PCR (qRT-PCR) were performed using the Power Syber Green Master Mix (Applied Biosystems, cat. no. 4368708) in a StepOne Plus RT-PCR apparatus (Applied Biosystems). Gene expression was assessed by the comparative CT (ΔΔCt) method with β-actin as the reference gene. The following primers were used: *Snail2fwd* GATGCGCTCGCAGTGATAGT; *Snail2rev* AGCTTTCATACAGGTATGGGGATA; *Sox10fwd* CGGAGCACTCTTCAGGTCAG; *Sox10rev* CCCTTCTCGCTTGGAGTCAG; *Foxd3fwd* TCTGCGAGTTCATCAGCAAC; *Foxd3rev* TTCACGAAGCAGTCGTTGAG; *Glut1fwd* AAGATGACAGCTCGCCTGATG; *Glut1rev* AGTCTTCAATCACCTTCTGCGG; *PFKPfwd* TTGGAATTGTCAGCTGCCCG; *PFKPrev* TGCAGACAACTTTCATAGGCATCAG; *βActinfwd* CTGTGCCCATCTATGAAGGCTA; *βActinrev* ATTTCTCTCTCGGCTGTGGTG.

Immunofluorescence Labeling of Cultures

For immunolabeling, the following primary antibodies were used: Rabbit monoclonal antibody (mAb) to Snail-2 (clone C19G7, Cell Signaling, 1/300), mouse mAb to Sox-10 (Clone A2, Santa Cruz, 1/200), mouse mAb to β-catenin (clone 14, BD-Transduction Laboratories, 1/200), mouse mAb to paxillin (Clone 165, BD-Transduction Laboratories, 1/100), mouse mAb to α-SMA conjugated to Cy3 (Clone 1A4, Sigma, 1/300), mouse mAb to βIII-tubulin conjugated to Alexa488 (Clone Tuj-1, R&D Systems, 1/500), mouse mAb to HNK-1 described previously ((Tucker et al., 1984), undiluted culture supernatant), mouse mAb to MITF (clone C5, Abcam, 1/200), and mouse mAb to Glut-1 (Ab14683, Abcam, 1/50). Filamentous actin was detected using Texas Red™-X Phalloidin

(Molecular probe, cat. no. T7471). NCC primary cultures were performed in 4-well plates or in 8-well chambered glass coverslips (Nunc, cat. no. 154511) coated with fibronectin, and fixed in 4% paraformaldehyde (PFA) in PBS for 15 minutes at room temperature for detection of all antigens, except for Snail-2 (5 minutes in 4% PFA), β-catenin (45 minutes in 1.5% PFA), and Glut-1 (see below). After permeabilization with 0.5% Triton X-100 in PBS for 5 minutes, cultures were blocked in PBS-3% BSA and subjected to immunofluorescence labeling using primary antibodies followed by incubation with appropriate secondary Ab conjugated to Alexa-fluor 488, Cy-3 or Cy-5 (Jackson Immunoresearch Laboratories), and processed for DAPI or Hoechst staining to visualize cells' nuclei before mounting in ImmuMount medium (Shandon). For Glut-1 labeling, unfixed NCC cultures were incubated with the Glut-1 antibody diluted in DMEM for 15 minutes at 15°C to avoid antibody internalization and immediately fixed in 100% ethanol at -20°C before rinsing in PBS and secondary antibody treatment. Preparations were observed with a Zeiss AxioImager M2 epifluorescence microscope equipped with 10X-63X fluorescence objectives (Acroplan 10X/0.25, 20X/0.45, Plan-Neofluar 40X/0.75 and 63X/1.25 oil) or with a Zeiss LSM 900 confocal microscope equipped with 10X-40X fluorescence objectives (Plan-Apochrome 40X/1.30 oil). Data were collected using the Zen or Airyscan2 software and processed using ImageJ software. For each series of experiments, images were acquired using equal exposure times and settings.

2-NDBG Uptake

For 2-NDBG uptake in life embryos, portion of stage HH13-14 quail embryos taken from the last 10 formed somites and similar portion of the unsegmented mesoderm were cut and incubated at 37°C for 2 h into 100 µl of 1.5 mM 2-NDBG (Life technologies) solution in glucose and pyruvate-free medium placed in a suspension culture dish. After culture, embryos were fixed in 4% PFA for 20 min, and then washed with PBS for 5 min at least 3 times, positioned on microscope slide into an Immumount (Shandon) droplet, covered with a coverslip. For 2-NDBG uptake in cell cultures, NT explants were incubated at 37°C for 2 h in 100 µl of 1.5 mM 2-NDBG solution in DMEM without glucose and pyruvate, fixed in 4% PFA for 20 min, and mounted as for immunolabelings in ImmuMount. Embryos and cultures were imaged using a Zeiss AxioImager M2 epifluorescence microscope.

In Situ Hybridization for MRNA Detection on NCC Primary Cultures and Whole Mount Embryos

The following plasmids for mRNA probe synthesis were used: *Snail-2* from A. Nieto, *Foxd-3* from C. Erickson, *Sox-10* from P. Scotting, *Glut-1*, *PFK*, *PGK-1* and *PKM* from O. Pourquié. Linearized plasmid DNA was used to synthesize digoxigenin-UTP (Roche) labeled antisense probes with RNA polymerases from Promega and RNA probes were purified with Illustra ProbeQuant G-50 microcolumns (GE Healthcare). ISH were performed either on NCC primary cultures produced in fibronectin-coated plastic dishes or on whole mount intact embryos collected at the appropriate developmental stages, using essentially the same procedure. Samples of embryos and cultures were fixed in 4% PFA in PBS for 2 h at room temperature or overnight at 4°C. They were hybridized overnight at 65°C with the digoxygenin-UTP-labeled RNA probes in 50% formamide, 10% dextran sulfate and Denhart's buffer (0.5 μg probe/ml hybridization buffer) and washed twice in 50% formamide, 1x SSC and 0.1% Tween-20 at 65°C, then 4 times at room temperature in 100 mM maleic acid, 150 mM NaCl pH 7.5 and 0.1% Tween-20 (MABT buffer). After a 1-h pre-incubation in MABT buffer containing 10% blocking reagent (Roche) and 10% heat-inactivated lamb serum, samples were incubated overnight at room temperature with the anti-digoxygenin antibody (Roche). After extensive rinsing with MABT buffer, they were preincubated in 100 mM NaCl, 50 mM $MgCl_2$, 1% Tween-20, and 25 mM Tris-HCl, pH 9.5, and stained with NBT-BCIP (Roche) following manufacturer's guidelines. Preparations were observed and imaged with a Nikon stereomicroscope and data analyzed with ImageJ software.

Cryosectioning

To obtain embryo sections following in situ hybridization, embryos were washed in PBS for 1 h at room temperature and in 15% sucrose solution overnight at 4°C. Next, they were incubated in 7.5% porcine gelatin (dissolved in 15% sucrose solution) for 2-3 h at 40°C, embedded in gelatin-sucrose in cup, snap-frozen in chilled isopentane at -70°C and stored at -80°C. 20-μm sections were obtained using the Leica cryostat and collected on Superfrost/Plus slides (Thermo Fisher Scientific). For imaging, the slides were immersed in PBS at 40°C for 2 h for gelatin removal, washed in PBS and mounted in Aquatex mounting medium (Merck). Preparations were observed and imaged with a Hamamatsu NanoZoomer Digital Slide Scanner and treated with NDP.View2 software.

Quantification of substrate and cell-cell adhesions

Several fields of paxillin or β-catenin immunofluorescent staining were selected randomly at the periphery of the NCC outgrowth over at least three different NT explants per condition in at least two independent experiments. Quantifications of number, area and aspect ratio of substrate adhesions were performed as follows: For each experiment, images were segmented by manual thresholding

using ImageJ. For each image, the area and aspect ratio of each single substrate adhesion were measured using ImageJ Analyse Particle plugin for particle size (micron):0.2-infinity. The number of substrate adhesion per NCC corresponds to the mean of all the ratios, obtained for the images of each NT explant, between the total number of substrate adhesions quantified in the image and the number of NCC present on the same image. Quantification of the number of substrate adhesion per NCC at 24 h was performed by manual counting on each image. Each dot represents the mean of substrate adhesion number counted per NCC per neural tube explant. Quantification of cell-cell contact numbers was performed as follows: For each experiment the number of contact each NCC engaged with its neighbors was counted manually on each image. The number of cell-cell adhesion engaged per NCC corresponds to the mean of the values obtained for the images of each NT explant. The data were expressed as percentage of NCC with zero to 3 contacts with their neighbors.

Cell Proliferation Assay

Cell proliferation in culture was monitored using the Plus EdU Cell proliferation kit for imaging from Life Technologies (cat. no. C10638). Briefly, NCC primary cultures were generated on fibronectin-coated glass coverslips as for immunolabelings and were incubated with EdU at 20 μM in culture medium for 1 h at varying times of NCC development. Immediately after EdU incorporation, cultures were fixed in 4% PFA in PBS for 15 minutes at room temperature, permeabilized in 0.5 Triton-X100 for 15 minutes and treated for EdU detection using Alexa-555 Fluor azide in accordance with the manufacturer's guidelines. After DNA staining with Hoechst, cultures were optionally processed for immunostaining and analyzed as described for immunolabelings.

Cell Locomotion Assays

NCC primary cultures were performed in 8-well chambered glass coverslips coated with fibronectin. Up to 4 NT explants were distributed separately into each well, and were maintained at 37°C in a humidified 5%-CO_2 incubator for about 2 h until the NT adhered firmly to the dish and NCC initiated migration on the substratum; then the cultures were transferred into a heated chamber (Ibidi) with a humid atmosphere containing 5% CO_2/95% air placed on the motorized stage of a Leica DMIRE2 microscope equipped with a CoolSNAP HQ camera (Roper Scientific). Time-lapse video-microscopy was performed with a 10x objective and phase contrast images were captured every 5 minutes during 16-24 h using the Micromanager software. The progression of the migratory front of the NCC population every hour was measured using a custom GUI written in Matlab® (MathWorks®, Natick, Massachusetts, USA). Trajectories and positions of individual NCC in several explants recorded in parallel were tracked using Metamorph 7 software. The velocity of each NCC was calculated as the

ratio between the total length of its trajectory and the duration of the acquisition time. The persistence of movement was calculated as the ratio between the linear distance from the NCC's initial to final positions and the total distance covered by the cell. Evolution of speed and persistence every hour were calculated as the length of NCC trajectory per 1 h and the persistence of movement as the ratio between the linear distance from the cell's initial to final positions at each hour and the total distance covered by the cell during the corresponding period.

Preparation of polyacrylamide gels

Polyacrylamide (PAA) gels were prepared on 32-mm glass coverslips and 8-well chambered glass coverslips for AFM and TFM experiments, respectively. The surface on which the PAA gels were polymerized was activated by immersion into a solution of 3-methacryloxypropyltrimethoxysilane (0.3%, Bind-Silane, Sigma, cat. no. 440159), 10% acetic acid aqueous solution (3%) in absolute ethanol during 3 minutes to enhance gel adhesion, washed 3 times with ethanol, and air-dried for 45 minutes. Thin sheets of PAA gel of different elastic properties were prepared from concentrations of acrylamide/bisacrylamide 5%/0.225% and 3%/0.08%, supplemented with 0.5% ammonium persulfate and 0.05% tetramethylethylenediamine (Sigma) in H_20. Practically, for AFM experiments, 81 μl of these different mixtures were placed onto the surface of a 32 mm-diameter coverslip and covered with 14 mm-diameter coverslip. For immunostaining and video-microscopy experiments, 2.5 μl of the mixtures were placed in the wells of 8-well chambered glass coverslips and covered with a 6 mm-diameter coverslip. Top coverslips were treated previously with Repel-Silane ES (Merck, cat. no. GE17-1332-01) during 5 minutes to prevent PAA gel adhesion. After 30 minutes of polymerization, the top coverslips were removed and the PAA gels were rinsed 3 times with PBS, treated twice for 5 minutes with sulfo-SANPAH, UV-photoactivated with Bio-Link Crosslinker BLX-E254 (Biotech), and rinsed 3 times with 50 mM HEPES at pH 8.5. For traction force microscopy experiments, the gel mixtures contain FluoSpheres from Sigma (TM carboxylate modified, 0.2 μm, red (580/605), cat. no. F8810), at 1/50 dilution. A solution of fibronectin was layered onto the PAA gels at 30 μg/cm^2 and incubated overnight at 4°C under agitation.

AFM assessments on polyacrylamide gels and NCC

The elastic modulus for both PAA gels and NCC cultured for 4-6 h was assessed by AFM JPK NanoWizard Sence+ (Brucker, Billerica, Massachusetts, U.S.A) coupled to a Zeiss Axio-Observer z1 inverted microscope, as described previously (Ben Bouali et al., 2020) using μMash CSC38/NO AL probes (MikroMasch®, Sofia, Bulgaria). PAA gels and NCC were set in culture medium containing 25 mM HEPES and maintained at 37°C. For PAA gels, measurements were achieved

considering a measuring point grid with 0.4- μ m meshes over a 4.8×4.8 μ m² surface set in gel center. For NCC, measurements were achieved considering a measuring point grid with 1- μ m mesh over a 12×12 μ m² surface set on cells using visual inspection with a phase contrast microscope. Setting Poisson's ratio ν = 0.5 for both PAA gels and NCC, AFM spectroscopy curves were analyzed according to (Bilodeau, 1992), for quadrilateral pyramid probe using a home-written program in Matlab®. The elastic modulus of the PAA gels prepared with proportion of acrylamide/bisacrylamide 5%/0.225% and 3%/0.08% were of 6320 +/- 25 Pa and 1250 +/- 32 Pa (s.e.m), respectively, and were referred in the text as stiff and soft gels. The impact of PAA gels stiffness on Young's moduli values of NCC was measured by AFM and the obtained values were corrected as previously described (Rheinlaender et al., 2020).

TFM assessments

NT explants were cultured onto bead-embedded PAA gels in various nutrients for 4-6 h and transferred into a heated chamber with a humid atmosphere containing 5% CO_2/95% air placed on the motorized stage of a Zeiss LSM 900 confocal microscope. A specific injector connected to 8-well Chambered glass coverslips was designed for trypsin delivery and installed on the chambered glass coverslips. Images of bead positions were acquired using Plan-Apochrome 40X/1.30 oil objective as follows: Images with force were acquired with 2-min interval leading to a 12-min observation time before trypsinization (stress images) and one image was acquired without force (reference image) taken after NCC have detached by trypsinization and no longer exerting forces on the substrate. Confocal stress and reference images were aligned using a Matlab® script. The gel deformation was measured by the PIV (Particle Image Velocimetry) technique using the ImageJ plug-in PIV to get the bead displacement field. Finally, the ImageJ plug-in FTTC (Fourier Transform Traction Cytometry) was used to measure the traction force, exerted by NCC and responsible of PAA gel deformation and bead displacement (Martiel et al., 2015). The number of NCC in the traction force field was measured by counting NCC nuclei stained with NucSpot® Live 650 and a confocal image was generated before starting TFM measurements. The stress taken into account is the mean stress calculated from 6 couples of reference-stress images corresponding to 2, 4, 6, 8, 10 and 12 minutes TFM assessments. It was observed that between 2 and 12 minutes calculated stress was almost constant. The stress per cell is the stress divided by the number of nuclei. The force per cell (nN/cell) was calculated by multiplying the total stress/cell (Pa/cell) by the area of the interrogation window (μm²) used in the PIV.

Energy estimation

We estimated produced energy during NCC locomotion on soft and stiff gels by calculating the product of the average force F obtained by TFM and the average distance D covered per hour obtained by video-microscopy tracking during the time frame of TFM studies. The s.d. of the product F by D was calculated based on the following formula (Goodman, 1960): σ (F×D) = √(〖E(F)〗 ^2 〖 σ (D)〗 ^2+ 〖E(D)〗 ^2 〖 σ (F)〗 ^2+ 〖 σ (F)〗 ^2 〖 σ (D)〗 ^2), with σ the s.d. and E(F) and E(D) mean value of F and D respectively, assuming F and D with normal distribution. To evaluate the statistical significance of two energy values, i.e., $m_1 \pm \sigma_1$ and $m_2 \pm \sigma_2$, we calculated Student's t and degrees of freedom, $n_1 + n_2 - 2$, assuming $n_1 = n_2 = 5$ for size of m_1 and m_2, to obtain p values. For this, we considered $t = \frac{|m_1 - m_2|}{\sqrt{\frac{\sigma^2}{n_1} + \frac{\sigma^2}{n_2}}}$, and σ common s.d, given by $\sigma^2 = \frac{(n_1-1)\cdot\sigma_1^2 + (n_2-1)\cdot\sigma_2^2}{n_1+n_2-2}$.

Statistical Methods

Statistical analyses were performed using Prism 7 (GraphPad). For statistical analysis of data, we used One-way ANOVA parametric test after the validation of normality and equality of variances using Shapiro-Wilk and Brown-Forsythe methods, respectively. Otherwise, non-parametric Krustal-Wallis test was used. For comparison between two conditions we use unpaired t-test two-tailed test after the validation of normality and equality of using Shapiro-Wilk and equality of variances. Otherwise, non-parametric Mann-Whitney test was used. Unless specified, at least three independent experiments were carried out for each procedure. Each NT explant was considered as an individual sample. The data obtained for each drug or nutrient condition were compared to that of the medium without drug or with both nutrients, respectively. The n of samples (explants or embryos) analyzed is indicated in each graph in brackets. For statistical analysis of qRT-PCR results of in-vitro experiments, mRNA expression from a pool of 5-8 NT explants are presented as mean ± s.e.m of triplicates per experiment and gene. In *in-vivo* experiments, mRNA expression was measured per embryo after analyzing of three replicates measurements acquired per embryo and genes. The data obtained from embryos injected with drugs were analyzed using Two-way ANOVA relative to the data of embryos injected with vehicle. Data are expressed as mean values ± s.d. or s.e.m and the P values are * p<0.05, ** p<0.01; *** p<0.001; **** p<0.0001. Results are considered statistically significantly different when p<0.05.

ACKNOWLEDGMENTS

We deeply thank Chantal Thibert and Sakina Torch for providing advice in cellular metabolism and critical reading of the manuscript. Special thanks to Olivier Pourquié and Masayuki Oginuma for providing cDNA probes for chicken glycolytic enzymes. Many thanks to Xavier Decrouy from the IMRB imaging platform and Xavier Laffray from the histology and imaging platform of the Laboratoire Gly-CRRET for advice.

COMPETING INTERESTS

The authors declare no competing financial interests.

AUTHOR CONTRIBUTIONS

N.N.-M. performed experiments, analyzed data and contributed to the manuscript. R.F. provided expertise in biomechanics and performed experiments for AFM and TFM. S. F. provided expertise in biomechanics and prepared the PAA gels. A.D. provided expertise for *in ovo* studies and facilities for cryo-sectioning methods and analyses. M.D. performed NCC primary culture experiments. F.R. provided financial support. R.F. and R.M. provided expertise in cellular metabolism and Seahorse technology and revised the manuscript. J.-L.D. conceived and designed the experimental approach, performed experiments, analyzed the data, and wrote the manuscript. S.D. conceived and designed the experimental approach, performed experiments, analyzed the data, and contributed to the manuscript.

FUNDING

This work was supported by funding from Institut National de la Santé et de la Recherche Médicale, Université Paris-Est Créteil, AAP IMRB cross-teams project, and Fondation ARC pour la Recherche sur le Cancer (No. PJA 20181207844). N.N.-M. was funded by doctoral fellowship of Université Paris-Est Créteil and by the Labex REVIVE during the last year of her Ph.D. M.D. was funded by CDD contract of Agence Nationale de la Recherche (No. ANR-12-BSV2-0019).

DATA AVAILABILITY

All relevant data can be found within the article and its supplementary information.

REFERENCES

Barriga, E. H., Franze, K., Charras, G. and Mayor, R. (2018). Tissue stiffening coordinates morphogenesis by triggering collective cell migration in vivo. *Nature* **554**, 523-527.

Barriga, E. H. and Mayor, R. (2019). Adjustable viscoelasticity allows for efficient collective cell migration. *Semin Cell Dev Biol* **93**, 55-68.

Ben Bouali, A., Montembault, A., David, L., Von Boxberg, Y., Viallon, M., Hamdi, B., Nothias, F., Fodil, R. and Féréol, S. (2020). Nanoscale mechanical properties of chitosan hydrogels as revealed by AFM. *Prog Biomater* **9**, 187-201.

Bhattacharya, D., Azambuja, A. P. and Simoes-Costa, M. (2020). Metabolic reprogramming promotes neural crest migration via Yap/Tead signaling. *Dev Cell* **53**, 199-211.e6.

Bhattacharya, D., Khan, B. and Simoes-Costa, M. (2021). Neural crest metabolism: At the crossroads of development and disease. *Dev Biol* **475**, 245-255.

Bigarella, C. L., Liang, R. and Ghaffari, S. (2014). Stem cells and the impact of ROS signaling. *Development* **141**, 4206-18.

Bilodeau, G. G. (1992). Regular pyramid punch problem. *J Appl Mech* **59**, 519-523.

Boon, R., Silveira, G. G. and Mostoslavsky, R. (2020). Nuclear metabolism and the regulation of the epigenome. *Nat Metab* **2**, 1190-1203.

Bronner, M. (2018). Riding the crest for 150 years! *Dev Biol* **444 Suppl 1**, S1-s2.

Burstyn-Cohen, T. and Kalcheim, C. (2002). Association between the cell cycle and neural crest delamination through specific regulation of G1/S transition. *Develop. Cell* **3**, 383-395.

Chevalier, N. R., Gazguez, E., Bidault, L., Guilbert, T., Vias, C., Vian, E., Watanabe, Y., Muller, L., Germain, S., Bondurand, N. et al. (2016). How tissue mechanical properties affect enteric neural crest cell Mmigration. *Sci Rep* **6**, 20927.

Duband, J. L. (2010). Diversity in the molecular and cellular strategies of epithelium-to-mesenchyme transitions: Insights from the neural crest. *Cell Adh Migr* **4**, 458-82.

Duband, J. L., Dady, A. and Fleury, V. (2015). Resolving time and space constraints during neural crest formation and delamination. *Curr Top Dev Biol* **111**, 27-67.

Duband, J. L., Nekooie-Marnany, N. and Dufour, S. (2020). Establishing primary cultures of trunk neural crest cells. *Curr Protoc Cell Biol* **88**, e109.

Dupin, E., Calloni, G. W., Coelho-Aguiar, J. M. and Le Douarin, N. M. (2018). The issue of the multipotency of the neural crest cells. *Dev Biol* **444 Suppl 1**, S47-S59.

Erickson, A. G., Kameneva, P. and Adameyko, I. (2023). The transcriptional portraits of the neural crest at the individual cell level. *Semin Cell Dev Biol* **138**, 68-80.

Goodman, L. A. (1960). On the exact variance of products. *J Am Statist Ass* **55**, 708-713.

Gu, W., Gaeta, X., Sahakyan, A., Chan, A. B., Hong, C. S., Kim, R., Braas, D., Plath, K., Lowry, W. E. and Christofk, H. R. (2016). Glycolytic metabolism plays a functional role in regulating human pluripotent stem cell state. *Cell Stem Cell* **19**, 476-490.

Hamburger, V. and Hamilton, H. L. (1951). A series of normal stages in the development of the chick embryo. *J Morphol* **88**, 49-92.

Herrero-Mendez, A., Almeida, A., Fernández, E., Maestre, C., Moncada, S. and Bolaños, J. P. (2009). The bioenergetic and antioxidant status of neurons is controlled by continuous degradation of a key glycolytic enzyme by APC/C-Cdh1. *Nat Cell Biol* **11**, 747-52.

Hu, N., Strobl-Mazzulla, P. H. and Bronner, M. E. (2014). Epigenetic regulation in neural crest development. *Dev Biol* **396**, 159-68.

Ito, K. and Suda, T. (2014). Metabolic requirements for the maintenance of self-renewing stem cells. *Nat Rev Mol Cell Biol* **15**, 243-56.

Iyer, N. V., Kotch, L. E., Agani, F., Leung, S. W., Laughner, E., Wenger, R. H., Gassmann, M., Gearhart, J. D., Lawler, A. M., Yu, A. Y. et al. (1998). Cellular and developmental control of O2 homeostasis by hypoxia-inducible factor 1 alpha. *Genes Dev* **12**, 149-62.

Johnson, M. T., Mahmood, S. and Patel, M. S. (2003). Intermediary metabolism and energetics during murine early embryogenesis. *J Biol Chem* **278**, 31457-60.

Kaelin, W. G., Jr. and McKnight, S. L. (2013). Influence of metabolism on epigenetics and disease. *Cell* **153**, 56-69.

Khacho, M., Clark, A., Svoboda, D. S., Azzi, J., MacLaurin, J. G., Meghaizel, C., Sesaki, H., Lagace, D. C., Germain, M., Harper, M. E. et al. (2016). Mitochondrial dynamics impacts stem cell identity and fate decisions by regulating a nuclear transcriptional program. *Cell Stem Cell* **19**, 232-247.

Konrad, C., Kawamata, H., Bredvik, K. G., Arreguin, A. J., Cajamarca, S. A., Hupf, J. C., Ravits, J. M., Miller, T. M., Maragakis, N. J., Hales, C. M. et al. (2017). Fibroblast bioenergetics to classify amyotrophic lateral sclerosis patients. *Mol Neurodegener* **12**, 76.

Lempradl, A., Pospisilik, J. A. and Penninger, J. M. (2015). Exploring the emerging complexity in transcriptional regulation of energy homeostasis. *Nat Rev Genet* **16**, 665-81.

Li, Y., Vieceli, F. M., Gonzalez, W. G., Li, A., Tang, W., Lois, C. and Bronner, M. E. (2019). In vivo quantitative imaging provides insights into trunk neural crest migration. *Cell Rep* **26**, 1489-1500 e3.

Lukoseviciute, M., Gavriouchkina, D., Williams, R. M., Hochgreb-Hagele, T., Senanayake, U., Chong-Morrison, V., Thongjuea, S., Repapi, E., Mead, A. and Sauka-Spengler, T. (2018). From pioneer to repressor: bimodal Foxd3 activity dynamically remodels neural crest regulatory landscape in vivo. *Dev Cell* **47**, 608-628.e6.

Marchant, C. L., Malmi-Kakkada, A. N., Espina, J. A. and Barriga, E. H. (2022). Cell clusters softening triggers collective cell migration in vivo. *Nat Mater* **21**, 1314-1323.

Martiel, J.-L., Leal, A., Kurzawa, L., Balland, M., Wang, I., Vignaud, T., Tseng, Q. and Théry, M. (2015). Measurement of cell traction forces with ImageJ. *Methods Cell Biol* **125**, 269-287.

Martik, M. L. and Bronner, M. E. (2017). Regulatory logic underlying diversification of the neural crest. *Trends Genet* **33**, 715-727.

Mercier-Letondal, P., Marton, C., Godet, Y. and Galaine, J. (2021). Validation of a method evaluating T cell metabolic potential in compliance with ICH Q2 (R1). *J Transl Med* **19**, 21.

Miyazawa, H. and Aulehla, A. (2018). Revisiting the role of metabolism during development. *Development* **145**.

Monier-Gavelle, F. and Duband, J.-L. (1995). Control of N-cadherin-mediated intercellular adhesion in migrating neural crest cells in vitro. *J. Cell Sci.* **108**, 3839-3853.

Morriss, G. M. and New, D. A. (1979). Effect of oxygen concentration on morphogenesis of cranial neural folds and neural crest in cultured rat embryos. *J Embryol Exp Morphol* **54**, 17-35.

Nieto, M. A. (2002). The Snail superfamily of zinc-finger transcription factors. *Nat. Rev. Mol. Cell Biol.* **3**, 155-166.

Oginuma, M., Moncuquet, P., Xiong, F., Karoly, E., Chal, J., Guevorkian, K. and Pourquie, O. (2017). A gradient of glycolytic activity coordinates FGF and Wnt signaling during elongation of the body axis in amniote embryos. *Dev Cell* **40**, 342-353 e10.

Patra, K. C. and Hay, N. (2014). The pentose phosphate pathway and cancer. *Trends Biochem Sci* **39**, 347-54.

Pavlova, N. N. and Thompson, C. B. (2016). The emerging hallmarks of cancer metabolism. *Cell Metab* **23**, 27-47.

Perestrelo, T., Correia, M., Ramalho-Santos, J. and Wirtz, D. (2018). Metabolic and mechanical cues regulating pluripotent stem cell fate. *Trends Cell Biol* **28**, 1014-1029.

Rheinlaender, J., Dimitracopoulos, A., Wallmeyer, B., Kronenberg, N. M., Chalut, K. J., Gather, M. C., Betz, T., Charras, G. and Franze, K. (2020). Cortical cell stiffness is independent of substrate mechanics. *Nat Mater* **19**, 1019-1025.

Ridenour, D. A., McLennan, R., Teddy, J. M., Semerad, C. L., Haug, J. S. and Kulesa, P. M. (2014). The neural crest cell cycle is related to phases of migration in the head. *Development* **141**, 1095-103.

Rothstein, M. and Simoes-Costa, M. (2023). On the evolutionary origins and regionalization of the neural crest. *Semin Cell Dev Biol* **138**, 28-35.

Rovasio, R. A., Delouvee, A., Yamada, K. M., Timpl, R. and Thiery, J. P. (1983). Neural crest cell migration: requirements for exogenous fibronectin and high cell density. *J Cell Biol* **96**, 462-73.

Salazar-Roa, M. and Malumbres, M. (2017). Fueling the cell division cycle. *Trends Cell Biol* **27**, 69-81.

Santiago, A. and Erickson, C. A. (2002). Ephrin-B ligands play a dual role in the control of neural crest cell migration. *Development* **129**, 3621-32.

Schell, J. C., Wisidagama, D. R., Bensard, C., Zhao, H., Wei, P., Tanner, J., Flores, A., Mohlman, J., Sorensen, L. K., Earl, C. S. et al. (2017). Control of intestinal stem cell function and proliferation by mitochondrial pyruvate metabolism. *Nat Cell Biol* **19**, 1027-1036.

Schock, E. N. and LaBonne, C. (2020). Sorting Sox: Diverse roles for Sox transcription factors during neural crest and craniofacial development. *Front Physiol* **11**, 606889.

Schwarz, Q., Maden, C. H., Vieira, J. M. and Ruhrberg, C. (2009). Neuropilin 1 signaling guides neural crest cells to coordinate pathway choice with cell specification. *Proc Natl Acad Sci U S A* **106**, 6164-9.

Scully, D., Keane, E., Batt, E., Karunakaran, P., Higgins, D. F. and Itasaki, N. (2016). Hypoxia promotes production of neural crest cells in the embryonic head. *Development* **143**, 1742-52.

Semenza, G. L. (2012). Molecular mechanisms mediating metastasis of hypoxic breast cancer cells. *Trends Mol Med* **18**, 534-43.

Shellard, A. and Mayor, R. (2021). Collective durotaxis along a self-generated stiffness gradient in vivo. *Nature* **600**, 690-694.

Shyh-Chang, N., Daley, G. Q. and Cantley, L. C. (2013). Stem cell metabolism in tissue development and aging. *Development* **140**, 2535-47.

Simões-Costa, M. and Bronner, M. E. (2015). Establishing neural crest identity: a gene regulatory recipe. *Development* **142**, 242-57.

Simões-Costa, M. S., McKeown, S. J., Tan-Cabugao, J., Sauka-Spengler, T. and Bronner, M. E. (2012). Dynamic and differential regulation of stem cell factor FoxD3 in the neural crest is Encrypted in the genome. *PLoS Genet* **8**, e1003142.

Soldatov, R., Kaucka, M., Kastriti, M. E., Petersen, J., Chontorotzea, T., Englmaier, L., Akkuratova, N., Yang, Y., Haring, M., Dyachuk, V. et al. (2019). Spatiotemporal structure of cell fate decisions in murine neural crest. *Science* **364**.

Théveneau, E., Duband, J.-L. and Altabef, M. (2007). Ets-1 confers cranial features on neural crest delamination. *PLoS ONE* **2**, e1142.

Thiery, J. P., Duband, J.-L. and Delouvée, A. (1982). Pathways and mechanism of avian trunk neural crest cell migration and localization. *Develop. Biol.* **93**, 324-343.

Trainor, P. (2013). Neural Crest Cells: Evolution, Development and Disease: Elsevier.

Traxler, L., Lagerwall, J., Eichhorner, S., Stefanoni, D., D'Alessandro, A. and Mertens, J. (2021). Metabolism navigates neural cell fate in development, aging and neurodegeneration. *Dis Model Mech* **14**.

Tsogtbaatar, E., Landin, C., Minter-Dykhouse, K. and Folmes, C. D. L. (2020). Energy Metabolism Regulates Stem Cell Pluripotency. *Front Cell Dev Biol* **8**, 87.

Tucker, G. C., Aoyama, H., Lipinski, M., Tursz, T. and Thiery, J. P. (1984). Identical reactivity of monoclonal antibodies HNK-1 and NC-1: Conservation in vertebrates on cells derived from the neural primordium and on some leukocytes. *Cell Diff.* **14**, 223-230.

Vander Heiden, M. G., Cantley, L. C. and Thompson, C. B. (2009). Understanding the Warburg effect: the metabolic requirements of cell proliferation. *Science* **324**, 1029-33.

Vincent, M. and Thiery, J. P. (1984). A cell surface marker for neural crest and placodal cells: Further evolution in peripheral and central nervous system. *Develop. Biol* **103**, 468-481.

Zanotelli, M. R., Zhang, J. and Reinhart-King, C. A. (2021). Mechanoresponsive metabolism in cancer cell migration and metastasis. *Cell Metab* **33**, 1307-1321.

Zhang, J., Zhao, J., Dahan, P., Lu, V., Zhang, C., Li, H. and Teitell, M. A. (2018). Metabolism in pluripotent stem cells and early mammalian development. *Cell Metab* **27**, 332-338.

Zhu, J. and Thompson, C. B. (2019). Metabolic regulation of cell growth and proliferation. *Nat Rev Mol Cell Biol* **20**, 436-450.

FIGURE LEGENDS

Fig. 1. Glucose Metabolism is Required for Trunk NCC Development

(A) Whole mount views of the trunk of HH14 quail embryos: Left: hybridized with probes for *Glut-1*, *PFK*, *PGK-1*, *Foxd-3* and *Sox-10*, anterior to the top. *Foxd-3* and *Sox-10* mark the axial levels of NCC pre-migration (Foxd-3-low, Sox-10-low), delamination (Foxd-3-high, Sox-10-low), and migration (Foxd3-high, Sox-10-high) stages. Right: fluorescent glucose analog (2-NDBG) uptake with the intensity shown by pseudocolor image (16 colors; higher levels in red-yellow) using ImageJ, (n = 5). (B) Cross-sections through the last somites of whole mount ISH for *Glut-1*, *PFK*, *PGK-1*, and *Sox-10* showing the dorsal NT and delaminating (arrowhead) and early-migrating (arrow) NCC. The corresponding global views of the sections are shown in Fig. S1B. (C) Normalized levels of *Snail-2, Foxd-3* and *Sox-10* mRNAs in the trunk of embryos 5 h after 2-DG or vehicle (no-drug) injection measured by qRT-PCR. Measurements were done in triplicates per embryo and gene, analyzed by two-way ANOVA relative to the no-drug condition. (D) Whole mount views of the trunk of embryos 5 h, 24 h and 48 h after 2-DG or vehicle injection, hybridized with probes for *Foxd-3* and *Sox-10* or immunolabeled for HNK-1. Vertical bars delineate the axial levels where NCC development is defective. Arrowheads, arrows, and double arrows point at delaminating, migrating, and differentiating NCC, respectively. The corresponding global views of the embryos are shown in Fig. S2A. (E) Cross-sections through the caudal (left), mid (center), and anterior (right) trunk of embryos 24 h after 2-DG or vehicle injection and processed for whole mount ISH for *Sox-10*. Arrows point at NCC. (F) Overall aspect of trunk NT explants in 5 h and 24 h cultures in medium without glucose and pyruvate (no Gluc-no Pyr), with 5 mM glucose, 1 mM pyruvate, both, and in glucose and pyruvate medium with 2-DG. (G) Scatter plot with mean ± s.e.m. of NCC outgrowth area at 5 h and 24 h in conditions as in F, analyzed using one-way ANOVA followed by Dunnett's multiple comparison test relative to the condition with glucose and pyruvate. (H) Distance covered over time by the NCC migratory front in explants as in F and measured using video-microscopy. t0 corresponds to onset of recording 2-4 h after initiation of culture. 2-DG was applied immediately before recording. Front progression was analyzed using a custom GUI written in Matlab. Values are mean ± s.e.m. Data are from at least three independent experiments. Images in A, B, D, E, and F are from representative experiments. (n) indicate the number of embryos or explants analyzed. * $P<0.05$, ** $P<0.01$, *** $P<0.001$, **** $P<0.0001$; ns, not significantly different, $P>0.05$. Scale bars in A, 200 μm; B, 100 μm; D, 200 μm; and E and F, 100 μm. ao, aorta, dmt, dermamyotome; ec, ectoderm; pm, unsegmented paraxial mesoderm; sc, sclerotome; so, somite.

Fig. 2. Trunk NCC display a Typical OXPHOS Signature during Dispersion

(A) OCR and ECAR profiles in mitochondrial stress assays of individual trunk NT explants cultured for 5 h in medium with glucose, pyruvate, or both, using a Seahorse analyzer and analyzed using GraphPad Prism. (B) Energetic maps of 5 h-trunk and cranial explants in indicated nutrient conditions (left) and of 5 h- and 24 h-trunk explants in medium with glucose and pyruvate (right). (C) OCR and ECAR profiles of 5 h-trunk explants in glucose and pyruvate medium before and after addition of metabolic inhibitors. (D) Energetic maps of 5 h-explants in indicated nutrient conditions and in glucose and pyruvate medium with inhibitors. (E-G) Scatter plots of the OCR/ECAR ratio (E) and intracellular ATP level (F), and diagram of extracellular lactate produced (G) in 5h-trunk explants in indicated nutrient conditions and in glucose and pyruvate medium with inhibitors. Scatter plots with mean ± s.e.m. were analyzed using one-way ANOVA followed by Dunnett's multiple comparison test relative to the condition with glucose and pyruvate. Data in A-F and in G were collected from at least three and two independent experiments, respectively. (n) indicate the number of explants analyzed. Error bars in A-D and G are s.d. * $P<0.05$, ** $P<0.01$, **** $P<0.0001$; ns, not significantly different, $P>0.05$.

Fig. 3. OXPHOS Plays a Critical Role in Trunk NCC Development

(A) Normalized levels of *Snail-2, Foxd-3* and *Sox-10* mRNAs in the trunk of embryos 5 h after oligomycin or vehicle (no-drug) injection measured by qRT-PCR. Measurements were done in triplicates per embryo and gene, analyzed by two-way ANOVA relative to the no-drug condition. (B) Whole mount views of the trunk of embryos 5 h, 24 h and 48 h after oligomycin or vehicle injection, hybridized for *Foxd-3* and *Sox-10* or immunolabeled for HNK-1. Vertical bars delineate the axial levels where NCC development is defective. Arrowheads, arrows, and double arrows point at delaminating, migrating, and differentiating NCC, respectively. The corresponding global views of the embryos are shown in Fig. S4A. (C) Cross-sections of whole mount ISH for *Sox-10* through the caudal (left), mid (center), and anterior (right) trunk of embryos 24 after oligomycin or vehicle injection. Arrows point at NCC. (D) Overall aspect of NT explants in 5 h and 24 h cultures in glucose and pyruvate medium with metabolic inhibitors. (E) Scatter plot with mean ± s.e.m. of NCC outgrowth area at 5 h and 24 h in conditions as in D, analyzed using one-way ANOVA followed by Dunnett's multiple comparison test relative to the condition with glucose and pyruvate. (F) Distance covered over time by the NCC migratory front in NT explants cultured as in D and subjected to video-

microscopy. t0 corresponds to onset of recording 2-4 h after initiation of culture. Inhibitors were applied immediately before t0. Front progression was analyzed using a custom GUI written in Matlab. Values in A and F are mean ± s.e.m. Data are from at least three independent experiments. Images in B, C, and D are from representative experiments. (n) indicate the number of explants analyzed. * P<0.05, *** P<0.001, **** P<0.0001; ns, not significantly different, P>0.05. Scale bars in B, 200 μm; and C, D, 100 μm. ao, aorta, dmt, dermamyotome; ec, ectoderm; pm, unsegmented paraxial mesoderm; sc, sclerotome; so, somite.

Fig. 4. Glucose oxidation is required for *Snail-2* expression during trunk NCC delamination

(A) Scatter plot of the NCC production duration from NT explants in indicated nutrient conditions and in glucose and pyruvate medium with metabolic inhibitors. (B) Schematic description of the delamination assay. (C) Scatter plot of the number of delaminated NCC per explant in indicated nutrient conditions and in glucose and pyruvate medium with metabolic inhibitors. (D) Immunofluorescence staining for Snail-2 in delaminated (delam.) and migrating (migr.) NCC in conditions as in C. (E) Scatter plot of the proportion of Snail-2+ NCC in delaminated cells per explant in conditions as in C. The scatter plots with mean ± s.e.m. were analyzed using one-way ANOVA followed by Dunnett's multiple comparison test and relative to the medium in both nutrients without inhibitor. (n) indicate the number of explants analyzed. (F) Normalized levels of *Snail-2* mRNAs measured by qRT-PCR in explants in conditions as in C except that the NT was not removed before mRNA extraction. Measurements were done in triplicates per condition and gene, and analyzed using unpaired t-test two-tailed, and expressed as mean ± s.e.m. (n) indicate the number of experiments. (G) ISH for *Snail-2* mRNAs in trunk NT explants in conditions as in F. Arrowheads point at pre-migratory NCC in the dorsal NT and arrows point at delaminated NCC in either sides of the NT. Data were collected from at least three independent experiments. Images in D and G are from representative experiments. * P<0.05, ** P<0.01, *** P<0.001, **** P<0.0001; ns, not significantly different, P>0.05. Scale bars in D and G, 50 and 100 μm, respectively.

Fig. 5. Glucose metabolism is crucial for Trunk NCC locomotion, adhesion and mechanical properties

(A-D) Effect of nutrients and metabolic inhibitors on NCC locomotion and adhesion: (A, B) Scatter plots of the velocity throughout the duration of the experiment (left) and graphs of the mean velocity over time (right) of individual NCC cultured in indicated nutrient conditions (A) and in glucose and pyruvate medium with inhibitors (B), as measured using video-microscopy using Metamorph. t0 corresponds to onset of recording 2-4 h after initiation of culture. Inhibitors were applied immediately

before recording. (C) Immunofluorescence staining for paxillin (green) with Dapi visualization of nuclei (blue) of NCC at 5 h in indicated nutrient conditions (left) and in glucose and pyruvate medium with metabolic inhibitors (right). (D) Scatter plots of the number of substrate adhesions normalized to NCC count at 5 h and 24 h in conditions as in C. (E-G) Effect of nutrients on NCC adhesion and migration on gels of different rigidities: (E, F) Scatter plots of the number of substrate adhesions normalized to NCC count at 5 h (E) and of velocity and persistence of individual NCC over 16 h (F) in culture on stiff (6.3 kPa) or soft (1.2 kPa) PAA-gels in indicated nutrient conditions. (G) Distance covered over time by the NCC migratory front in explants as in F, subjected to video-microscopy and measured using Matlab. (H-J) Effect of nutrients on trunk NCC mechanical properties on stiff and soft gels: (H) Scatter plot of NCC stiffness in 5-h cultures in the indicated nutrient and gel conditions. The green bars indicate the stiffness of the gels. (I) Merged images of phase contrast with fluorescent for Red-stained nuclei and pseudo-color traction map images of NCC in indicated conditions. Higher traction levels are in orange-yellow. (J) Scatter plot of NCC traction activity expressed as stress per individual cell. Each dot represents the average stress obtained from an independent TFM assessment on a NCC outgrowth, divided by the number of cell nuclei. Scatter plots with mean ± s.e.m. were analyzed using one-way ANOVA followed by Dunnett's multiple comparison test, relative to glucose and pyruvate medium without inhibitor (A-D), or relative to condition on stiff gel (E-J). * $P<0.05$, ** $P<0.01$, **** $P<0.0001$; ns, not significantly different, $P>0.05$. In A, B and F, (n) indicate the number of NCC analyzed in several explants, with for each explant 20 cells analyzed at the periphery of the outgrowth. In C-E and G, (n) indicate the number of explants, and in H, the number of NCC analyzed. Data presented were from at least three independent experiments. Error bars are s.e.m. Images in C, D, and I are from representative experiments. Scale bars in C, D, 20 μm; and I, 50 μm.

Fig. 6. Glucose and Pyruvate Differently Influence Trunk NCC Pluripotency and Differentiation Potential

(A, C) Immunofluorescence staining for Sox-10 in migrating NCC (A) and in delaminated (delam.) vs. migrating (migr.) NCC (green, with Dapi visualization of nuclei in blue, C), after 5-h cultures in indicated nutrient conditions and in glucose and pyruvate medium with inhibitors. (B, D) Normalized levels of *Foxd-3* and *Sox-10* mRNAs in explants cultured for 5 h as in A and C, measured by qRT-PCR. Measurements were done in triplicates per embryo and gene, analyzed by using unpaired t-test two-tailed, and presented as mean ± s.e.m. (n) indicate the number of experiments. (E) ISH for *Foxd-3* mRNAs in NT explants cultured for 5 h in indicated nutrient conditions and in glucose and pyruvate medium with inhibitors. Arrowheads point at pre-migratory NCC in the dorsal NT and arrows point at delaminated NCC in either sides of the NT. (F) Scatter plots with mean ± s.e.m. of the proportion

of Sox-10+, HNK-1+, Tuj-1+, MITF+, and α-SMA+ NCC in explants cultured for 1-3 days (d) under the indicated nutrient conditions, and analyzed using unpaired t-test two-tailed with the comparisons for each marker in one nutrient made relative to the condition with glucose and pyruvate at the same time. (n) indicate the number of explants analyzed. * P<0.05, ** P<0.01, *** P<0.001,**** P<0.0001; ns, not significantly different, P>0.05. Data were collected from at least three independent experiments. Images in A and C are from representative experiments. Scale bars in A, 50 μm; and C, 100 μm.

Fig. 7. Schematic representation of the integration of carbon metabolism in NCC development
During development, trunk NCC maximize the potential of the glucose pathway, so that they are endowed with the capacity to meet the high metabolic demands suitable for the coordinated execution of diverse cellular programs in a rapidly evolving environment: EMT, migration, proliferation, survival, adaptation to spatial and mechanical constraints, fate decision, and differentiation. This is achieved through the concerted and sustained mobilization of all metabolic pathways downstream of glucose uptake, including glycolysis, OXPHOS, and PPP, cooperating together to produce ATP and nucleotides as bioenergetic and biosynthetic supplies and possibly other metabolites such as NADP, NADPH and ROS. All together, these metabolites contribute to regulate gene networks, promote cytoskeletal network dynamics, and stimulate cell cycling and proliferation.

Distance covered by cells (μm/h ± s.d.)			
Glucose (Stiff)	69.25 ± 9.89	**Glucose (Soft)**	53.27 ± 9.27
Pyruvate (Stiff)	52.11 ± 3.98	**Pyruvate (Soft)**	44.46 ± 1.61
Glucose + Pyruvate (Stiff)	59.49 ± 7.50	**Glucose + Pyruvate (Soft)**	47.14 ± 8.03
Force / Cell (nN ± s.d.)			
Glucose (Stiff)	12.66 ± 3.56	**Glucose (Soft)**	14.59 ± 6.08
Pyruvate (Stiff)	17.62 ± 5.48	**Pyruvate (Soft)**	11.16 ± 7.25
Glucose + Pyruvate (Stiff)	14.14 ± 5.41	**Glucose + Pyruvate (Soft)**	6.90 ± 3.36
Energy / h (pJ ± s.d.)			
Glucose (Stiff)	0.88 ± 0.28	**Glucose (Soft)**	0.78 ± 0.36
Pyruvate (Stiff)	0.92 ± 0.30	**Pyruvate (Soft)**	0.50 ± 0.32
Glucose + Pyruvate (Stiff)	0.84 ± 0.34	**Glucose + Pyruvate (Soft)**	0.33 ± 0.17

Table I. Energy produced by trunk NCC on soft and stiff gels in different nutrient conditions

Energy (expressed in pJ/h) was calculated as the product of the average force/NCC (nN/cell; calculated by multiplying the total stress/cell (Pa/cell) by the area of the interrogation window (μm^2) used in the PIV) obtained by TFM and the average distance covered in μm during one hour. P values for glucose, pyruvate, and both between stiff and soft gels are 0.016, 0.063 and 0.636, respectively.

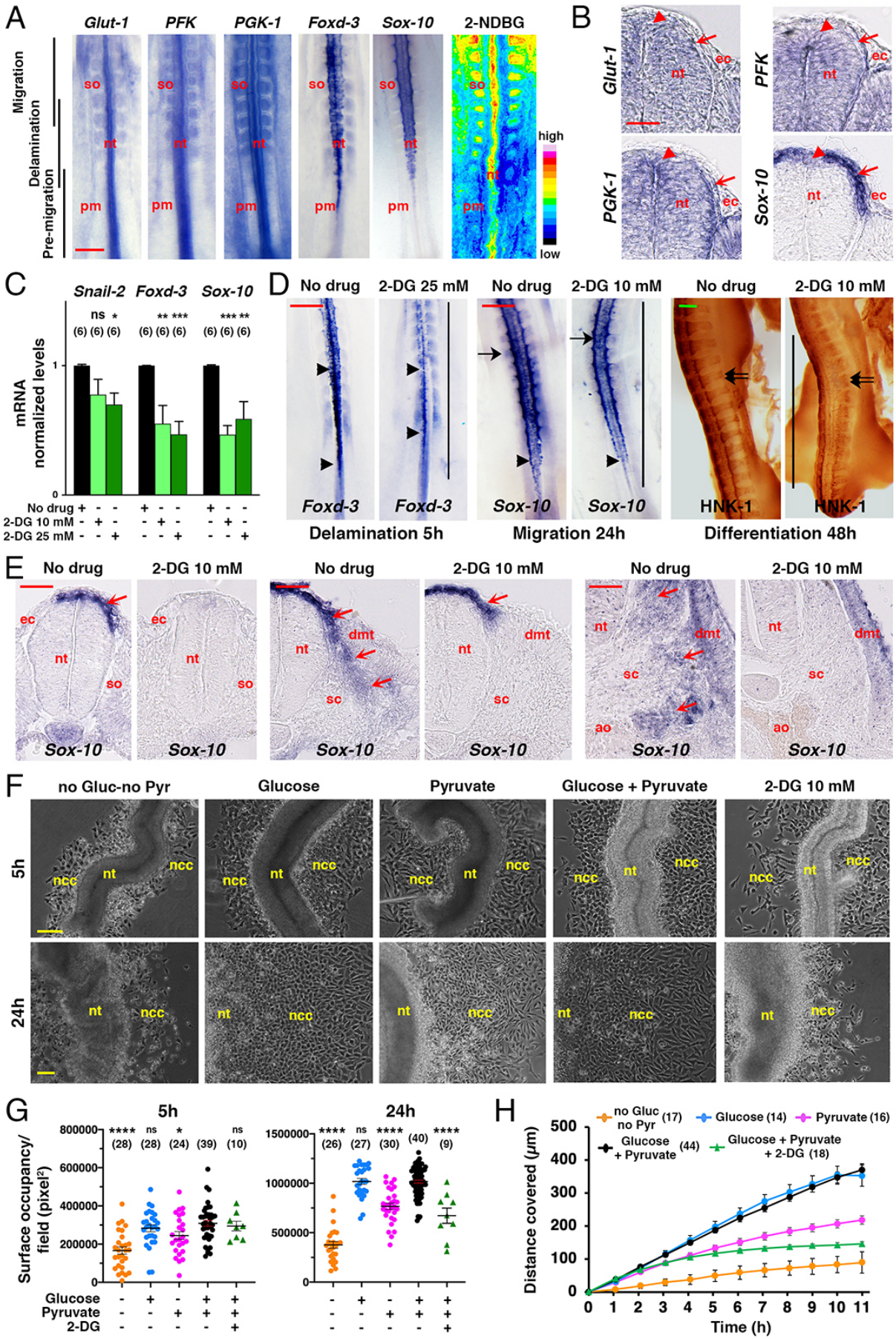

Figure 1: Nekooie-Marnany et al.

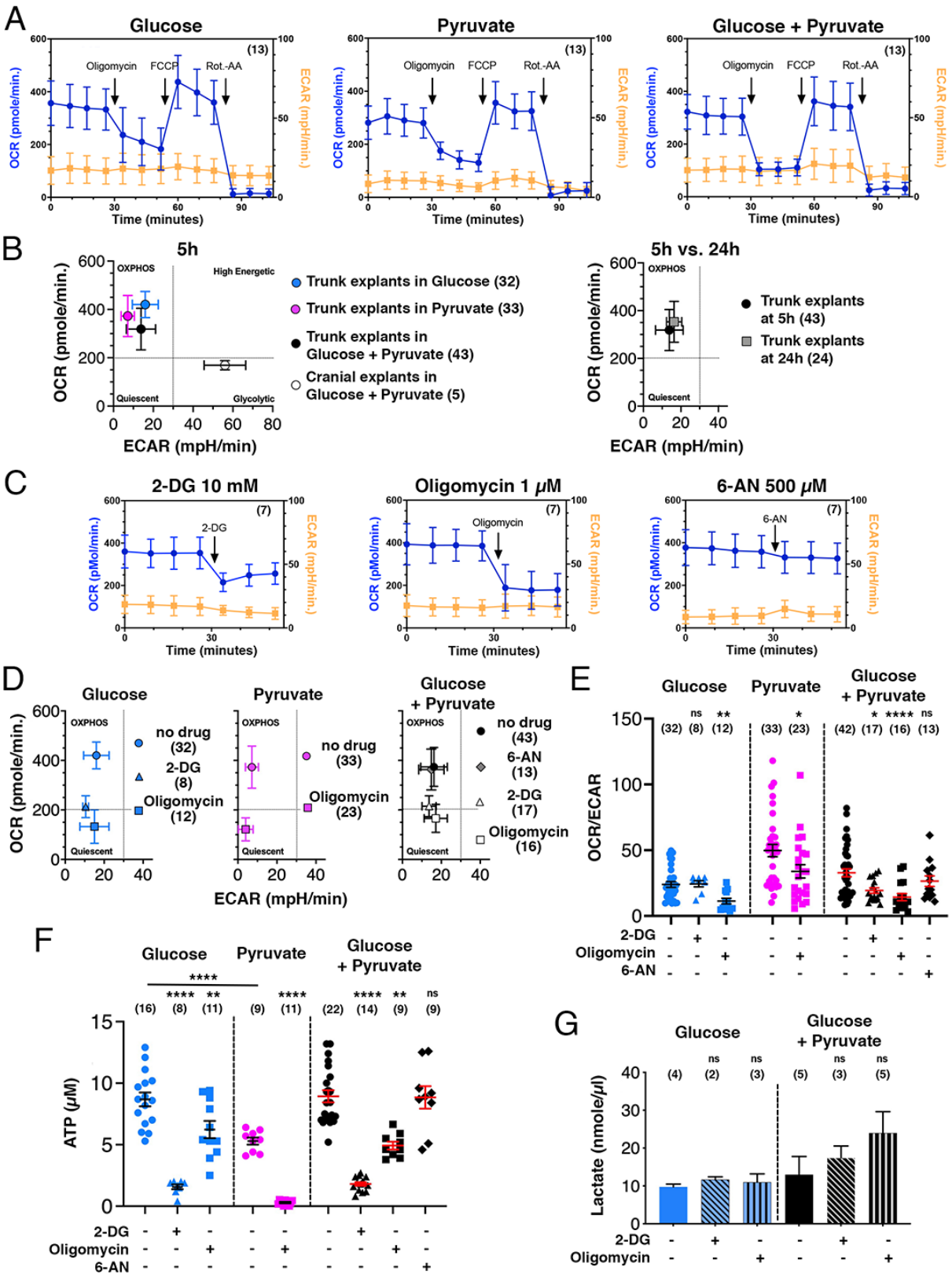

Figure 2: Nekooie-Marnany et al.

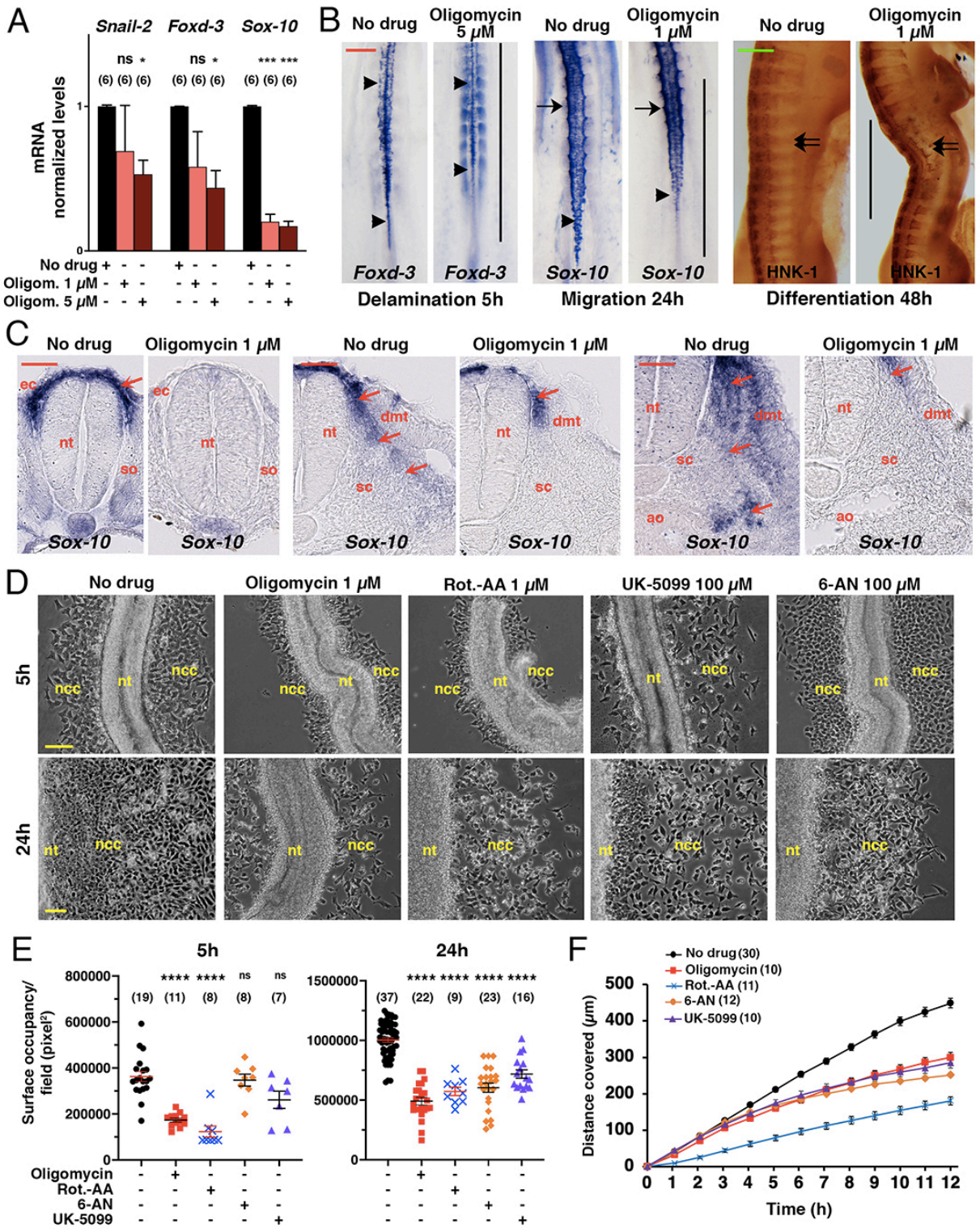

Figure 3: Nekooie-Marnany et al.

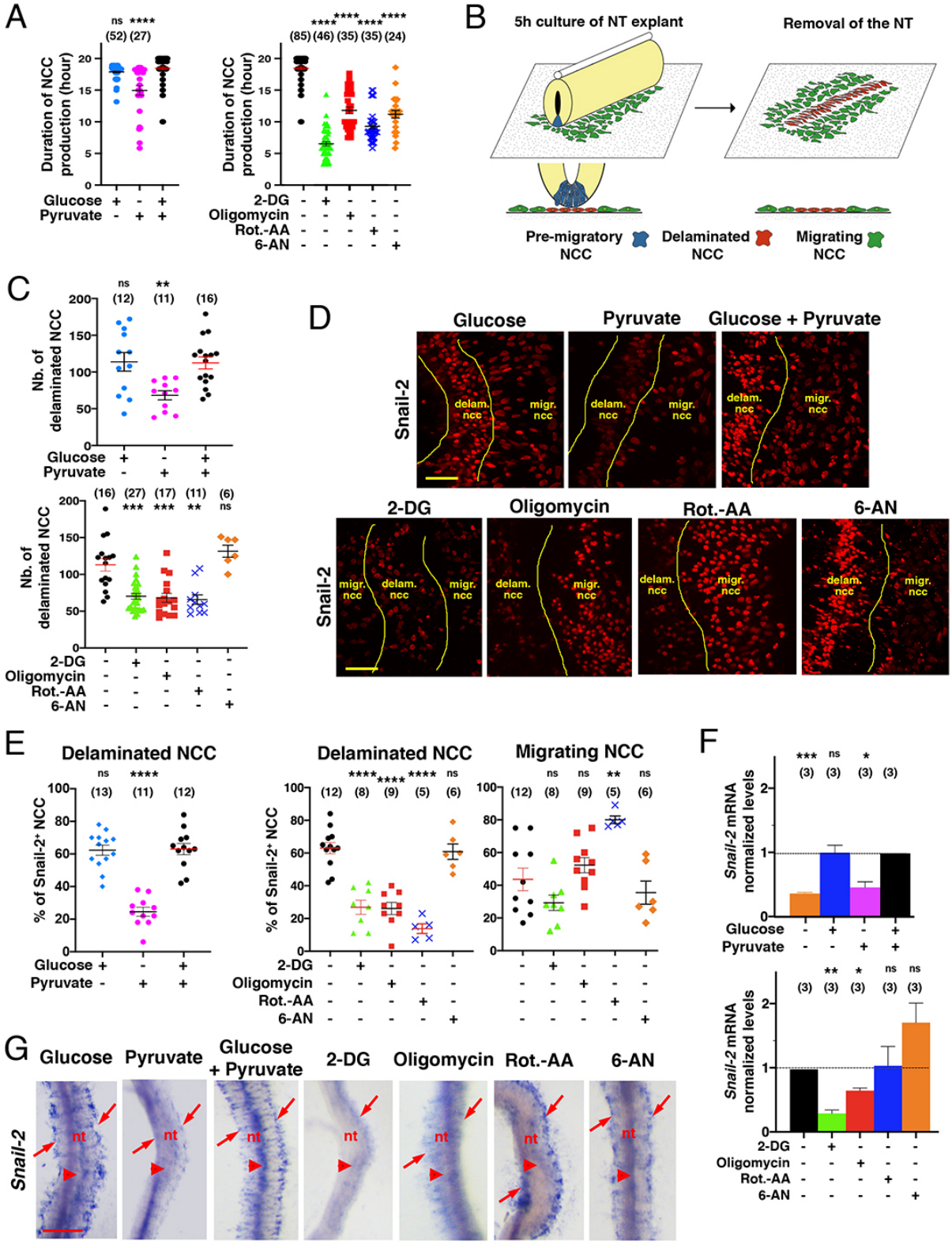

Figure 4: Nekooie-Marnany et al.

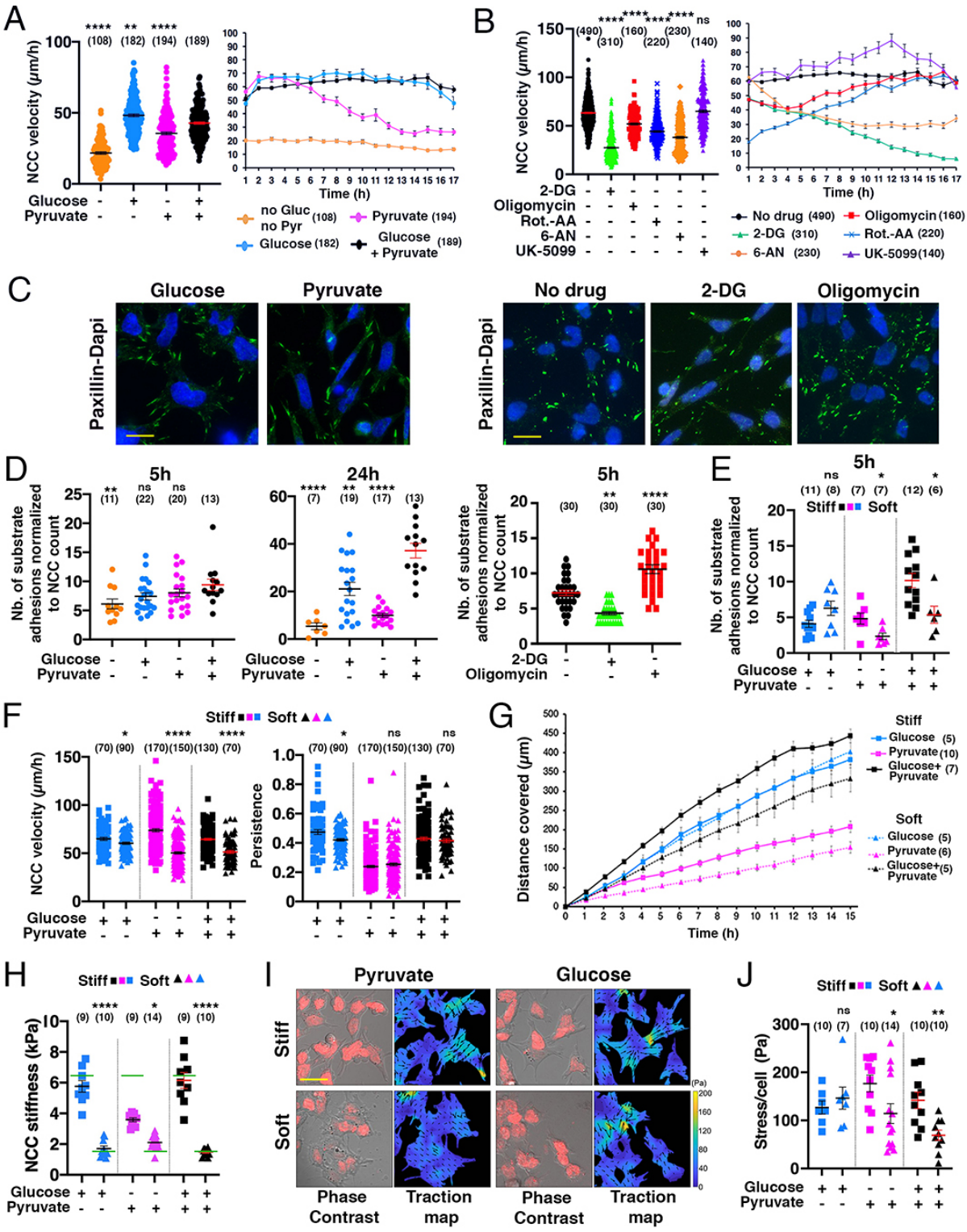

Figure 5: Nekooie-Marnany et al.

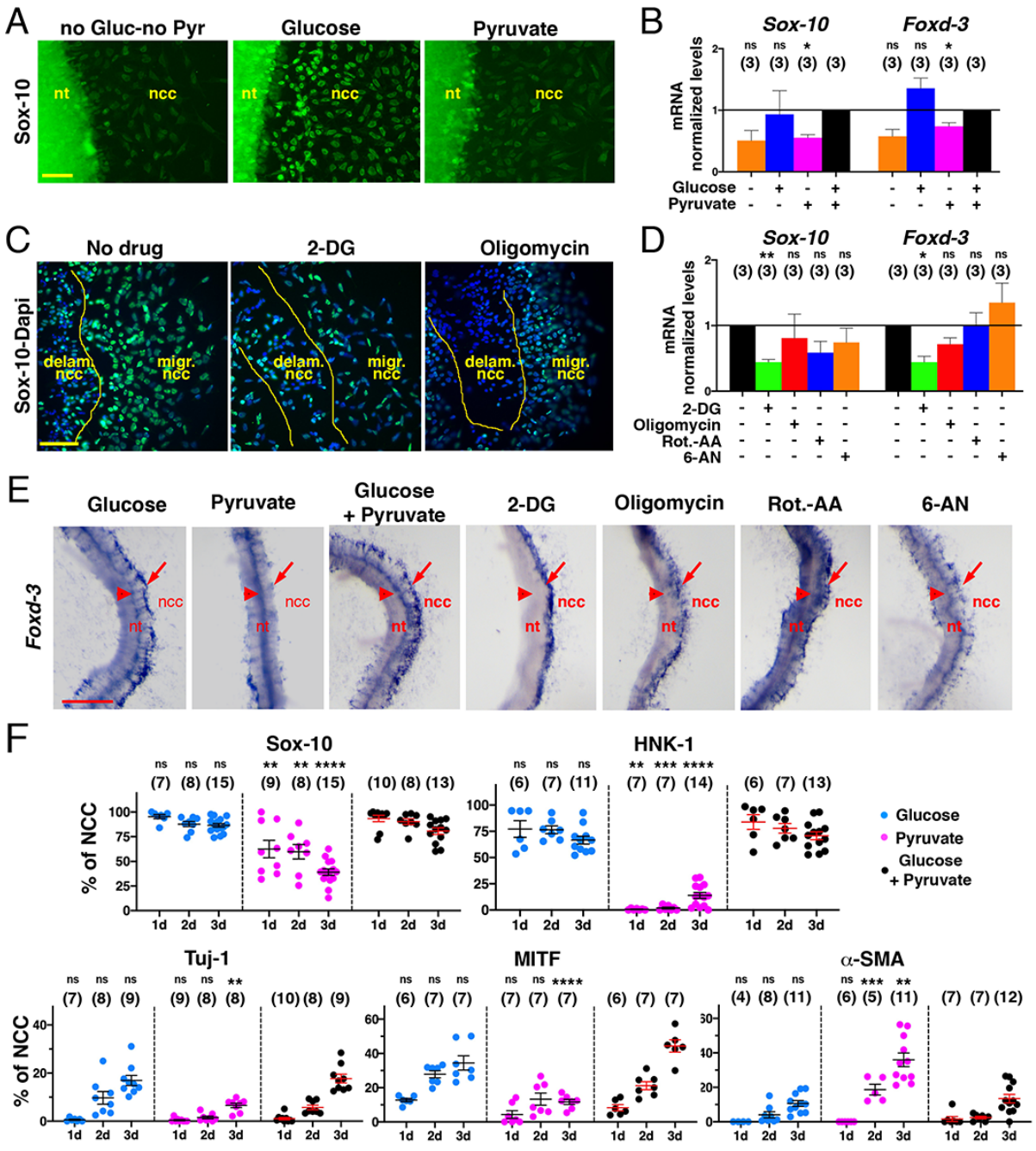

Figure 6: Nekooie-Marnany et al.

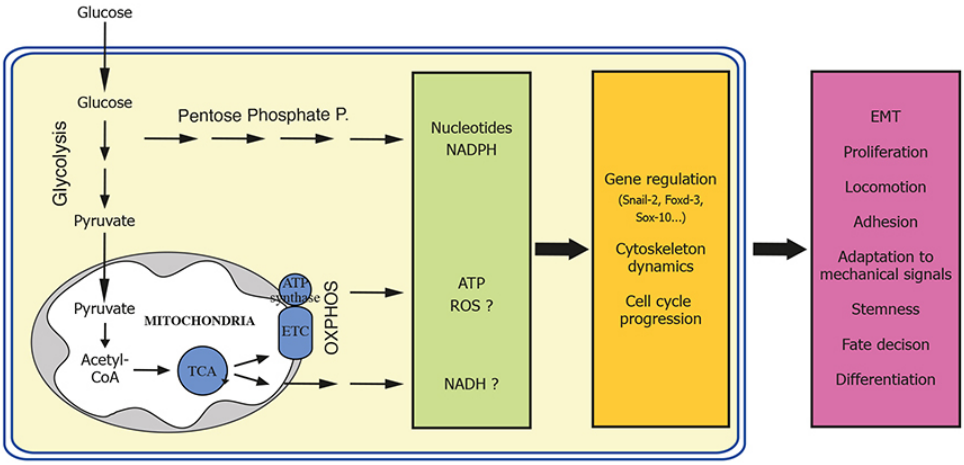

Figure 7: Nekooie-Marnany et al.

Supplementary Materials for

Glucose oxidation drives trunk neural crest cell development and fate

Nioosha Nekooie-Marnany, Redouane Fodil, Sophie Féréol, Alwyn Dady, Marine Depp#, Frédéric Relaix, Roberto Motterlini, Roberta Foresti, Jean-Loup Duband*, and Sylvie Dufour*

* Authors for correspondence: jean-loup.duband@inserm.fr and sylvie.dufour@inserm.fr

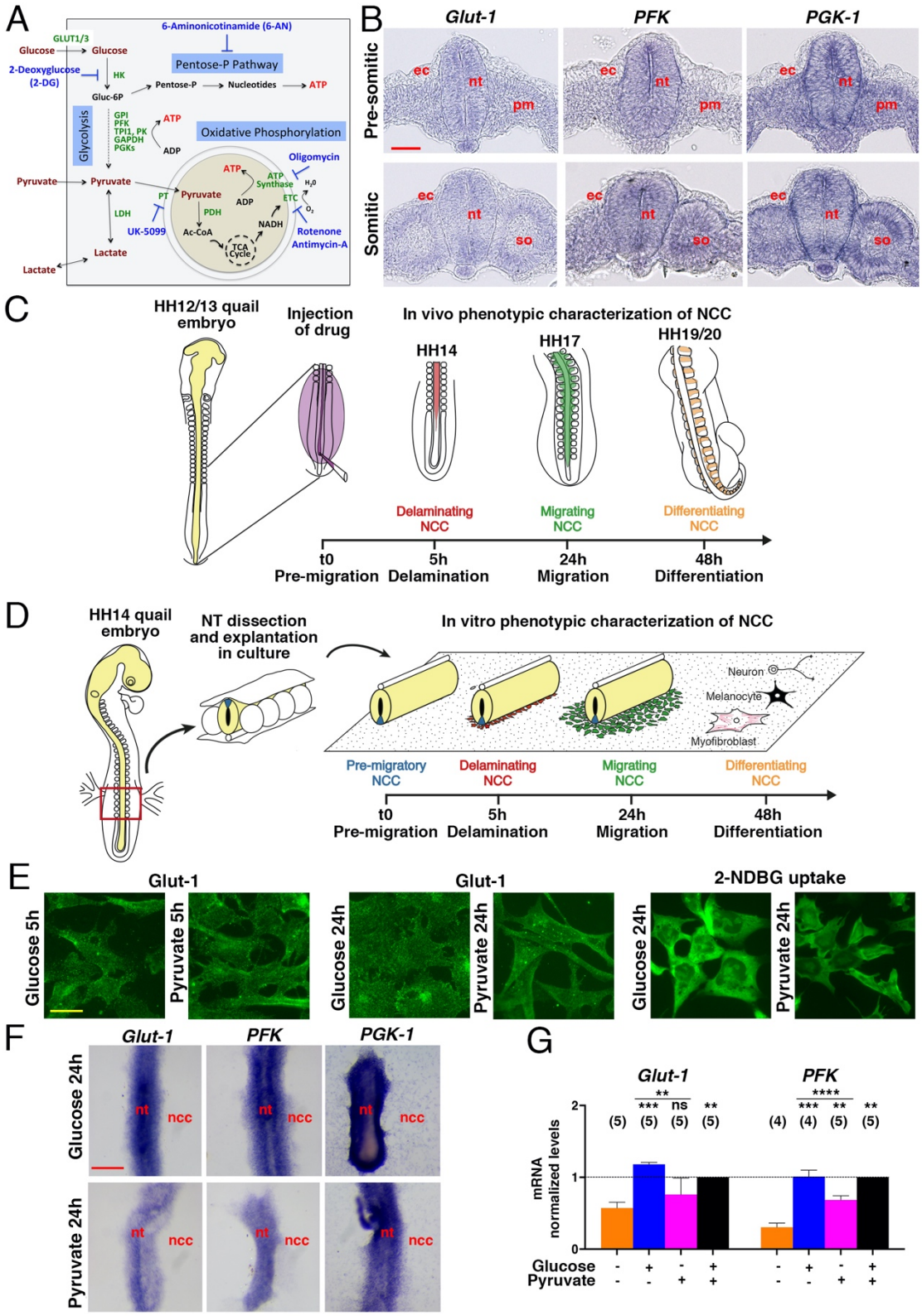

Supplementary Figure 1: Nekooie-Marnany et al.

Fig. S1, related to Fig.1.

(A) Representation of the main pathways of glucose and pyruvate metabolism indicating the specific targets of inhibitors of glycolysis (2-DG), ATP synthase (oligomycin), complex I-III of the electron transport chain (Rot.-AA), mitochondrial pyruvate transporter (UK-5099), and PPP (6-AN) used in this study. (B) Cross sections through the unsegmented paraxial mesoderm (pm) (upper panels) and the last somites (so) (lower panels) of embryos hybridized with probes for *Glut-1*, *PFK* and *PGK-1* mRNAs. The corresponding magnification views of the sections are shown in Fig. 1B. (C, D) Schematic representation of the procedure for *in-ovo* injection of quail embryos and *in vitro* culture of trunk NT explants, respectively, with indication of the timing of NCC development from pre-migration stage to early differentiation. (E) Left: Immunofluorescence staining for Glut-1 transporter on migrating NCC cultured in glucose or pyruvate medium for 5 h and 24 h. Right: Fluorescent 2-NDBG uptake performed on migrating NCC in glucose or pyruvate medium after 24-h culture. (F) ISH for *Glut-1*, *PFK*, and *PGK-1* mRNAs on 24 h-NT explants cultured in glucose or pyruvate. (G) Normalized levels. of *Glut-1* and *PFK* in NT explants at 24 h in indicated nutrient conditions measured by qRT-PCR. Measurements were done in triplicates per condition and gene, analyzed using unpaired t-test two-tailed relative to the conditions without glucose and pyruvate and that with both glucose and pyruvate, and presented as mean ± s.e.m. (n) indicate the number of experiments. Data were collected from at least three independent experiments. Images in B, E, and F are representative of these independent experiments. ** $P<0.01$, *** $P<0.001$, **** $P<0.0001$; ns, not statistically significant, $P>0.05$. Scale bars in B and F, 100 μm, and in E, 10 μm. ec, ectoderm; pm, unsegmented paraxial mesoderm; so, somite.

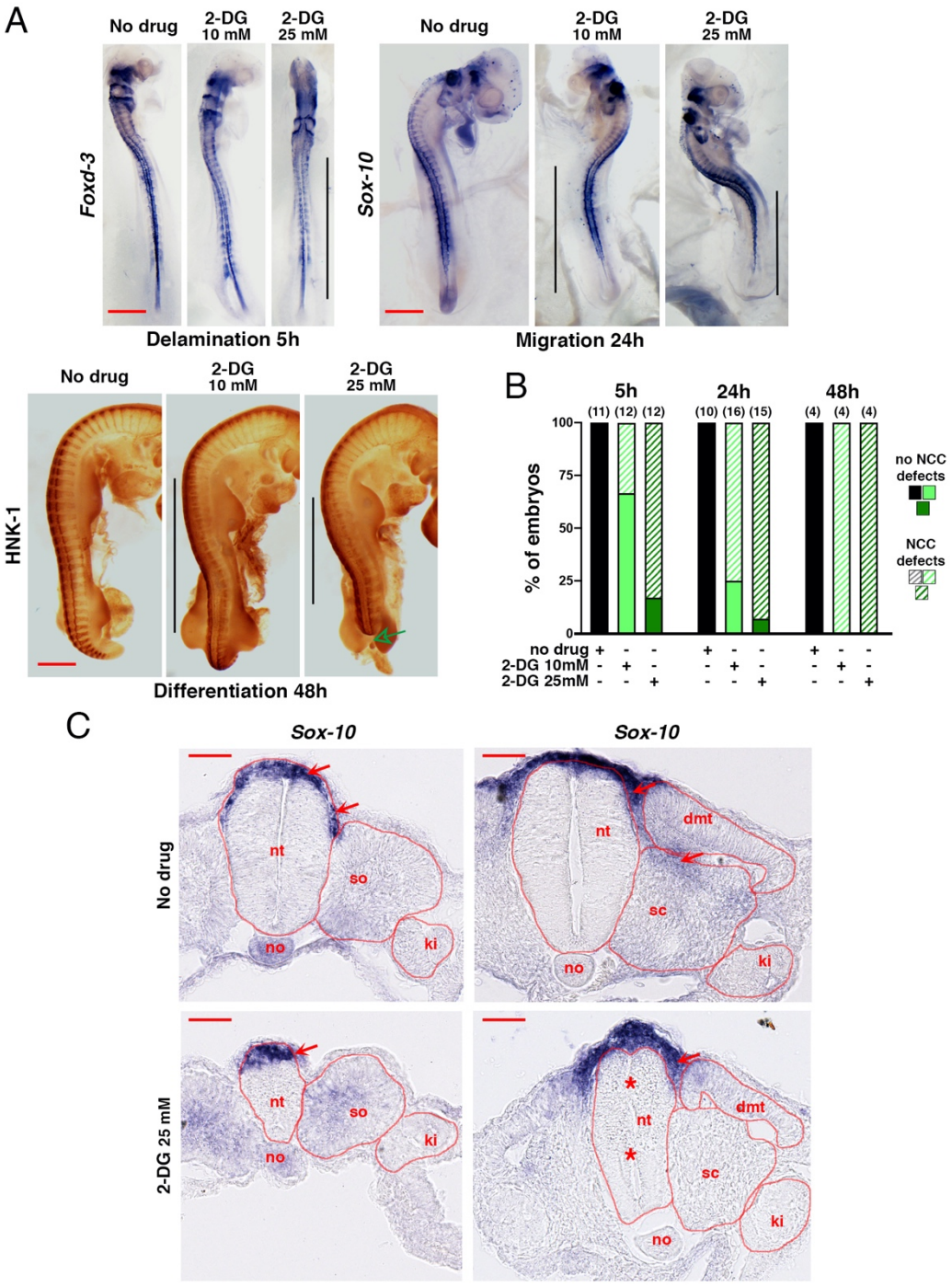

Supplementary Figure 2 : Nekooie-Marnany et al.

Fig. S2, related to Fig.1.

(A) Whole mount views of ISH with probes for *Foxd-3*, *Sox-10* mRNAs, and of immunolabeling for HNK-1, showing the whole embryo 5 h, 24h and 48 h after 2-DG or vehicle injection. Vertical bars delineate the axial levels where NCC development is defective. The green arrow points to the truncated tail of the embryo 48 h after treatment with 2-DG at 25 mM. Note that the cranial structures and NCC are not affected by caudal injection of 2-DG even at high concentrations. The corresponding views of the embryos at the trunk level are shown in Fig.1D. (B) Proportion of embryos with normal morphology (filled bars) or presenting with NCC defects (hatched bars), 5 h, 24 h and 48 h after injection with vehicle (black columns) or 2-DG at 10 mM (light green) and 25 mM (dark green). (C) Cross-sections through the caudal (left), and mid (center), trunk of embryos 24 h after injection with the vehicle (upper panels) or 2-DG at 25 mM (lower panels) and processed for whole mount ISH for *Sox-10*. Arrows point at NCC. The NT, somite, sclerotome, dermamyotome and kidney primordium have been circled to illustrate the reduced size and abnormal morphology of the axial and paraxial structures (NT and somites) compared with more lateral structure such as the kidney primordium in the presence of 2-DG. Asterisks indicate abnormalities in the NT lumen. Data were collected from at least three independent experiments. (n) indicate the number of embryo analyzed. Images in A and C are representative of at least three independent experiments. Scale bars in A, 500 μm; and C, 100 μm. ec, ectoderm; dmt, dermamyotome; no, notochord; pm, unsegmented paraxial mesoderm; sc, sclerotome; so, somite.

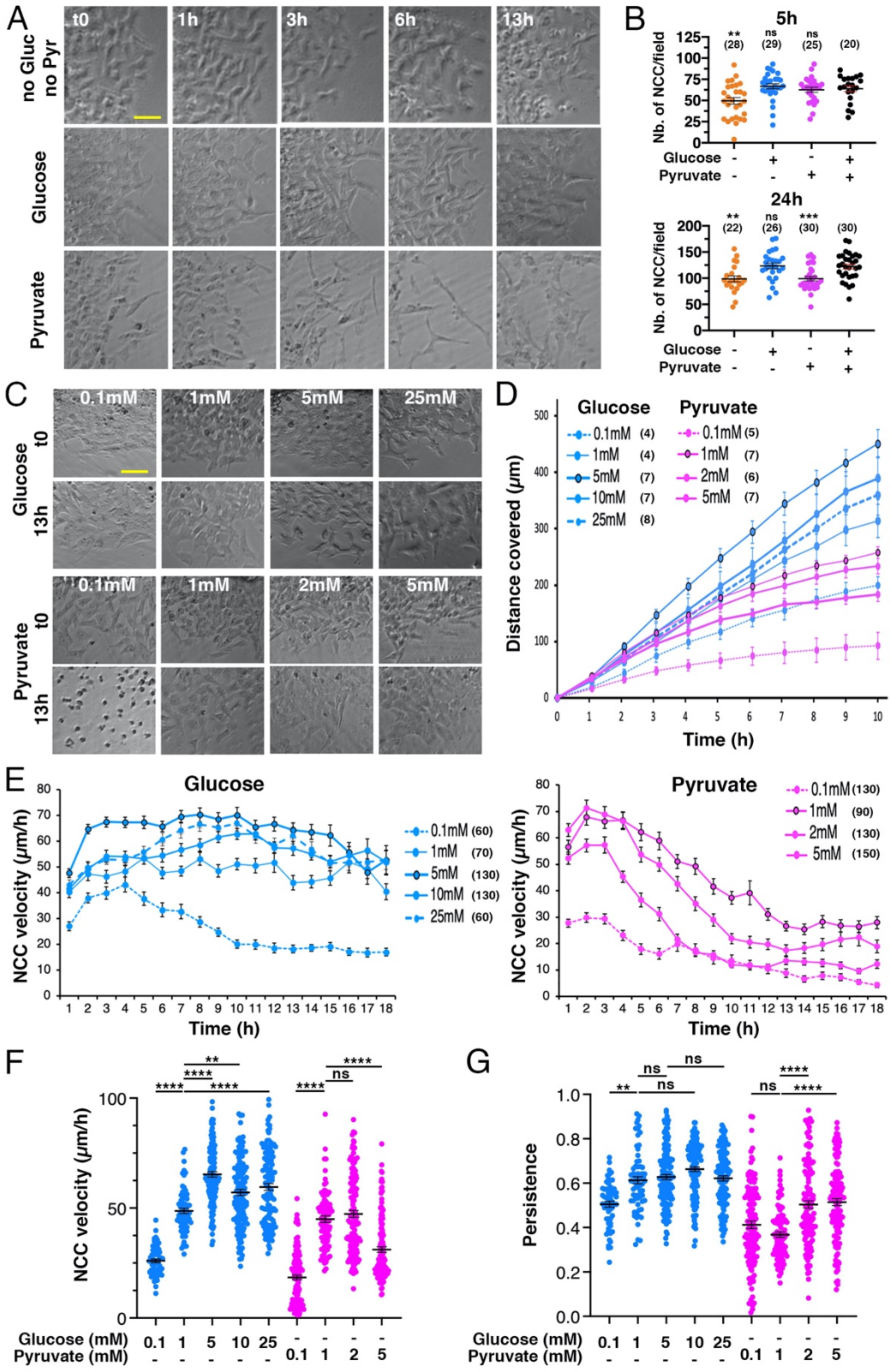

Supplementary Figure 3: Nekooie-Marnany et al.

65

Fig. S3, related to Fig.1.

(A) Morphological aspect of NCC at the migratory front at different time points of cultures in medium without glucose and pyruvate (no Gluc-no Pyr, top) or in the presence of 5 mM glucose or 1 mM pyruvate. Images were extracted from video-microscopic recordings performed as follows: trunk NT explanted in 8-well chambered glass coverslips coated with fibronectin and NCC were allowed to initiate outward migration for about 2-4 h before video-microscopy started, defined as t0. (B) Scatter plot with mean ± s.e.m of the cell density in NCC outgrowth at 5 and 24 h in conditions as in A, analyzed using one-way ANOVA followed by Dunnett's multiple comparison test relative to the glucose and pyruvate condition. (C) Morphological aspect of NCC at the migratory front at t0 and after 13 h in glucose or in pyruvate at different concentrations. Images were extracted from video-microscopic recordings as in A. (D) Curves of mean distance covered by the migratory front of the NCC population in medium with different glucose or pyruvate concentrations, analyzed throughout 10-h recording using a custom GUI written in Matlab. (E) Graphs of velocity of individual NCC over time in medium containing glucose or pyruvate at various concentrations throughout 18-h video-microscopy recordings, analyzed using Metamorph software. Values are mean ± s.e.m. and (n) indicate the total number of NCC analyzed in several NT explants with 20 NCC tracked at the periphery of the outgrowth on each side of NT. (F-G) Scatter plots with mean ± s.e.m of the velocity (F) and persistence (G) of individual NCC throughout the 18-h video microscopy recording, analyzed using one-way ANOVA followed by Dunnett's multiple comparison test. Data were collected from at least three independent experiments. Images in A and C are representative of at least three independent experiments. (n) indicate the number of trunk NT explants analyzed. In F and G, n are the same than those in E. ** $P<0.01$, *** $P<0.001$, **** $P<0.0001$; ns, not statistically significant, $P>0.05$. Scale bar in A and C = 50 μm.

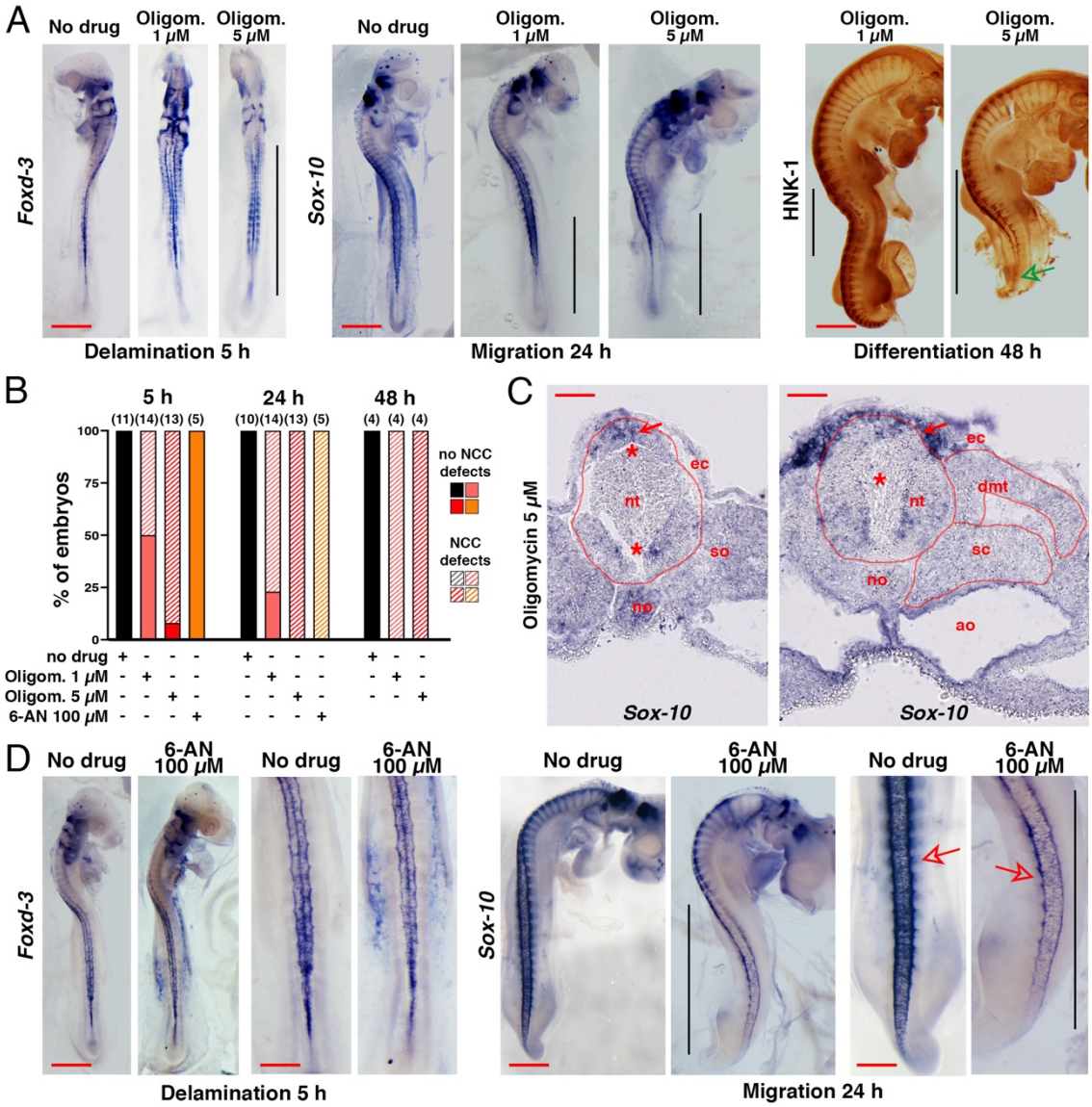

Supplementary Figure 4: Nekooie-Marnany et al.

90

Fig. S4, related to Fig. 3.

(A) Whole mount views of ISH with probes for *Foxd-3*, *Sox-10* mRNAs, and of immunolabeling for HNK-1, showing the whole embryo 5 h, 24h and 48 h after oligomycin or vehicle injection. Vertical bars delineate the axial levels where NCC development is defective. The green arrow points to the truncated caudal half of the embryo 48 h after treatment with oligomycin at 5 μM. Note that as for 2-DG, the cranial structures and NCC are not affected by caudal injection of oligomycin even at high concentrations. The corresponding views of the embryos at the trunk level are shown in Fig.3B. (B) Proportion of embryos with normal morphology (filled bars) or presenting with NCC defects (hatched bars), 5 h, 24 h and 48 h after injection with vehicle (black columns), oligomycin at 1 μM (light red columns) and 5 μM (dark red columns), or 6-AN at 100 μM (orange columns). (C) Cross-sections through the caudal (left), and mid (right) trunk of embryos 24 h after injection with oligomycin at 5 μM and processed for whole mount ISH for *Sox-10*. Arrows point at NCC. The NT, somite, sclerotome, and dermamyotome have been circled to illustrate the severe morphological alterations of the NT and somites. Asterisks indicate abnormalities in the NT lumen. (D) Whole mount views of ISH with probes for *Foxd-3*, *Sox-10* mRNAs, and of immunolabeling for HNK-1, showing the whole embryo (left panels for each probe) and detail of the trunk (right panels for each probe), 5 h, 24h and 48 h after 6-AN or vehicle injection. Vertical bars delineate the axial levels where NCC development is defective. The arrows point to migrating NCC. Data were collected from at least three independent experiments. (n) indicate the number of embryo analyzed. Images in A and C are representative of at least three independent experiments. Scale bars in A, 500 μm; in C, 100 μm; and in D, 500 μm for the overall views of embryos and 100 μm for the closer views of the trunk. ec, ectoderm; dmt, dermamyotome; no, notochord; pm, unsegmented paraxial mesoderm; sc, sclerotome; so, somite.

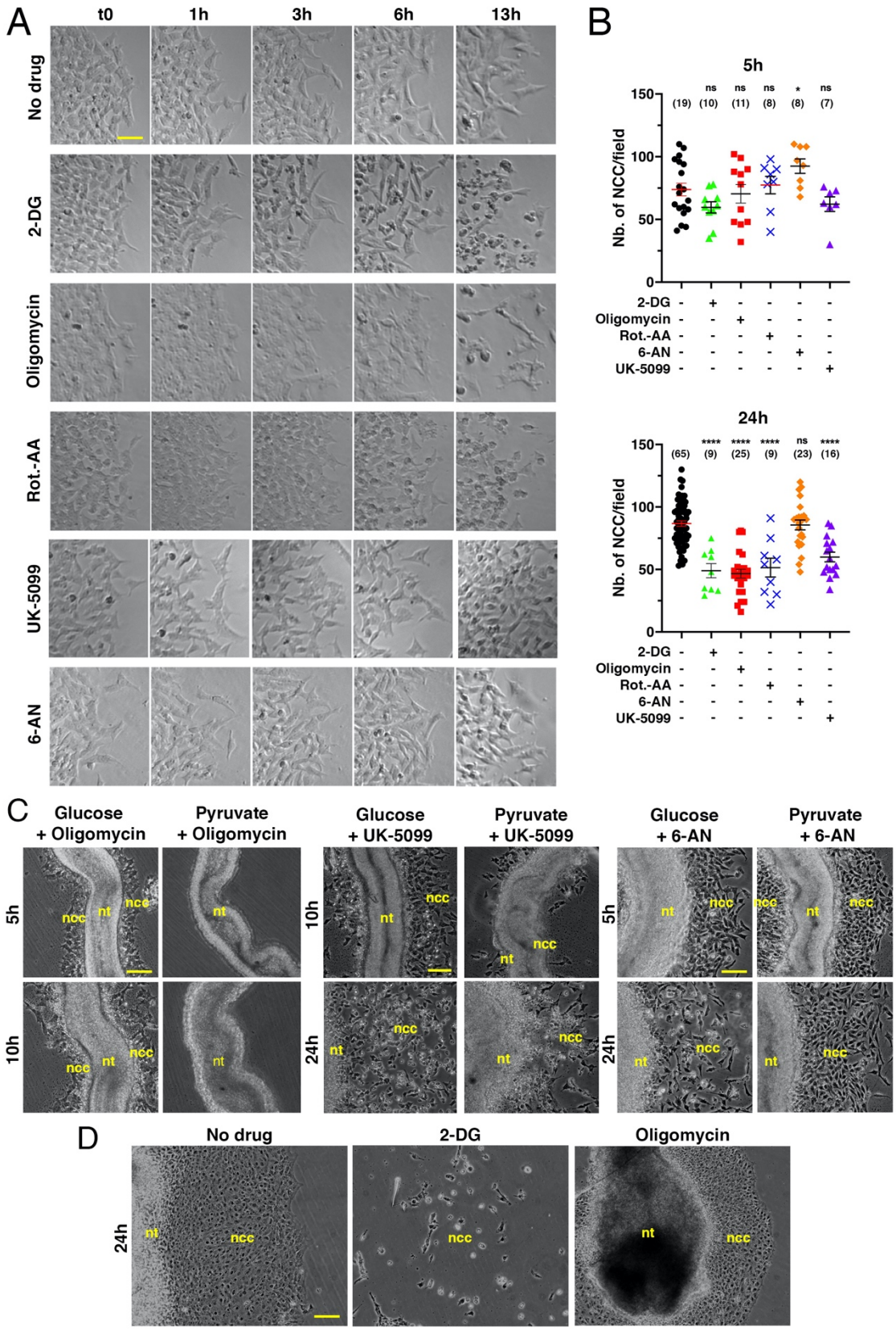

Supplementary Figure 5: Nekooie-Marnany et al.

114

Fig. S5, related to Fig. 3.

(A) Morphological aspect of NCC at the migratory front at different time points of cultures in glucose and pyruvate medium with metabolic inhibitors. Images were extracted from video-microscopic recordings performed as follows: trunk NT explanted in 8-well chambered glass coverslips coated with fibronectin and NCC were allowed to initiate outward migration for about 2-4 h before video-microscopy started, defined as t0. (B) Scatter plot with mean ± s.e.m of the cell density in NCC outgrowth at 5 and 24 h in conditions as in A, analyzed using one-way ANOVA followed by Dunnett's multiple comparison test relative to the glucose and pyruvate condition. (C) Overall aspect of trunk NT explants at different times in culture in medium with glucose alone or pyruvate alone in the presence of 1 μM oligomycin, 100 μM UK-5099, or 100 μM 6-AN. (D) Overall aspect of cranial NT explants at 24 h in medium with glucose and pyruvate (no drug) and in the presence of 1 mM 2-DG or 1 μM oligomycin. Data were collected from at least three independent experiments. Images in A, C and D are representative of at least three independent experiments. (n) indicate the number of trunk NT explants analyzed. ** $P<0.01$, *** $P<0.001$, **** $P<0.0001$; ns, not statistically significant, $P>0.05$. Scale bar in A, 50 μm; and in C, D, 100 μm.

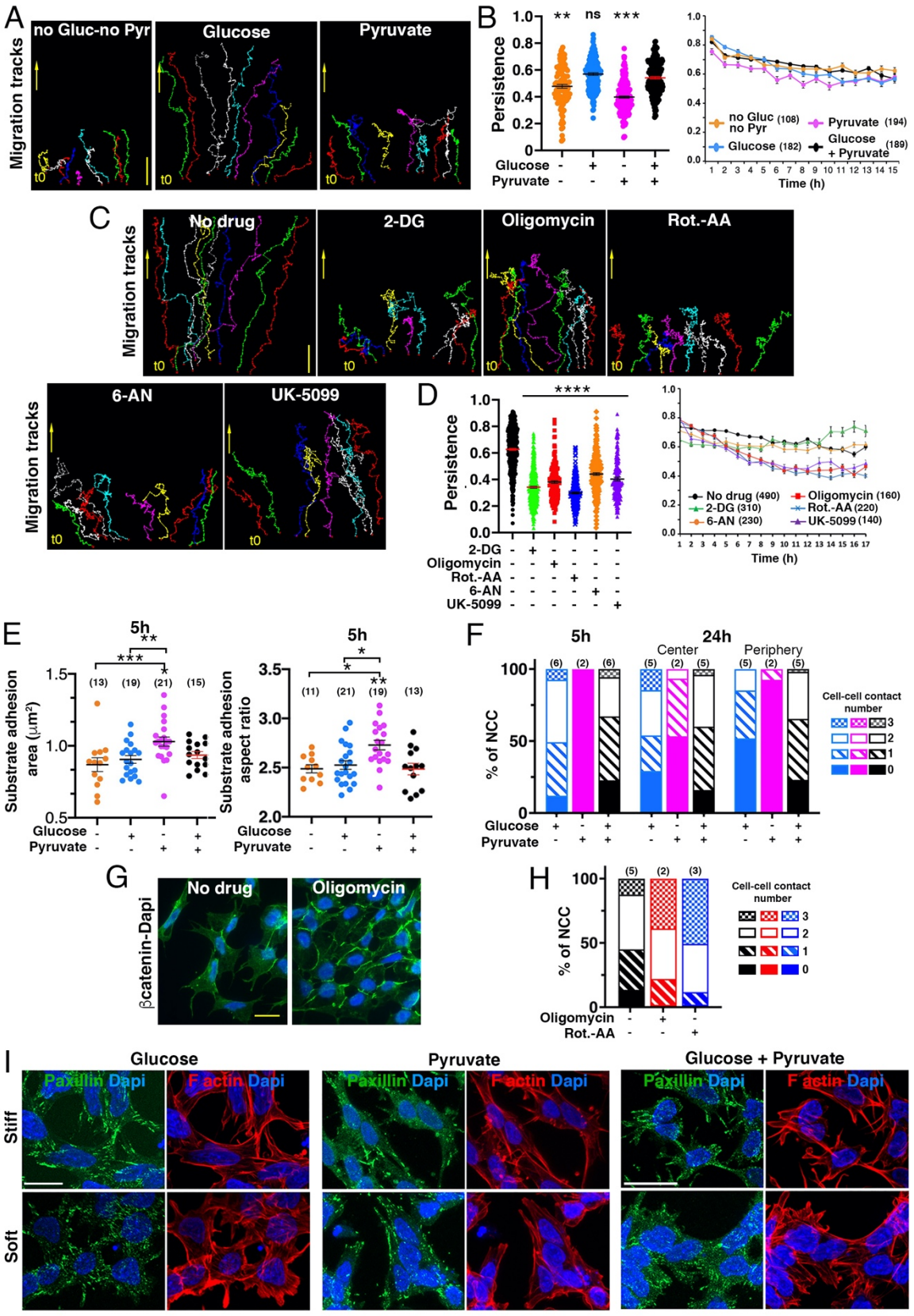

Supplementary Figure 6: Nekooie-Marnany et al.

131

Fig. S6, related to Fig. 5.

(A-D) Migration properties of NCC in various nutrients conditions and in the presence of metabolic inhibitors. (A, C) Migration tracks of several NCC from a representative NT explant in indicated nutrient conditions (A), or in glucose and pyruvate medium in the presence of metabolic inhibitors (C). NCC were allowed to initiate outward migration from trunk NT explants cultured in 8-well Chambered Coverglass for about 2-4 h before video-microscopy started, defined as t0. Drugs were added immediately before recording. The initial position of the cells is indicated at t0 and the direction of migration is given by the yellow arrow. (B, D) Scatter plots with mean ± s.e.m of the persistence (left) and curves of the persistence over time (right) of individual NCC expressed as with mean ± s.e.m throughout the video-microscopy recording in indicated nutrient conditions (B) or in glucose and pyruvate medium with metabolic inhibitors (D). (n) indicates the total number of NCC analyzed in several NT explants, with for each NT explant 20 NCC analyzed at the periphery of the outgrowth. (E) Scatter plot with mean ± s.e.m of the area of substrate adhesions (left) and their aspect ratio (right) in the indicated nutrient conditions. (F-H) Cell-cell adhesion properties of NCC in defined nutrient conditions and with metabolic inhibitors. (F) Number of cell-cell contacts formed by migrating NCC formed with their neighbors at 5 h, and at the center or the periphery of the outgrowth at 24 h. Data were obtained from images of trunk immunostained for β-catenin and are expressed as the proportions of NCC with 0-3 contacts/cell. (G) Immunolabeling for β-catenin (green) and nuclei visualization using Dapi (blue) in NCC cultured for 5 h in the presence of oligomycin compared with no drug condition. (H) Number of cell-cell contacts in migrating NCC cultured in glucose and pyruvate medium with metabolic inhibitors. Data were obtained and are expressed as in F. (I) Cell-substratum adhesion properties of NCC in defined nutrient conditions. Immunolabeling for paxillin (green), filamentous actin (red), and nuclei visualization using Dapi (blue) in NCC cultured for 5 h on stiff (6.3 kPa) and soft (1.2 kPa) PAA-gels coated with fibronectin in indicated nutrient conditions. Data were collected from at least three independent experiments. Images in A, C, G and I are from representative experiments. Scatter plots were analyzed using one-way ANOVA followed by Dunnett's multiple comparison test relative to the glucose and pyruvate condition (B, D) or to the medium with glucose alone (E). *P<0.05, **P<0.01, ***P<0.001,****P<0.0001; ns, not significant, P>0.05. Bars in A and C = 100 μm, G = 20 μm and I = 25 μm. Scale bar in A, 100 μm; and in G, I, 25 μm.

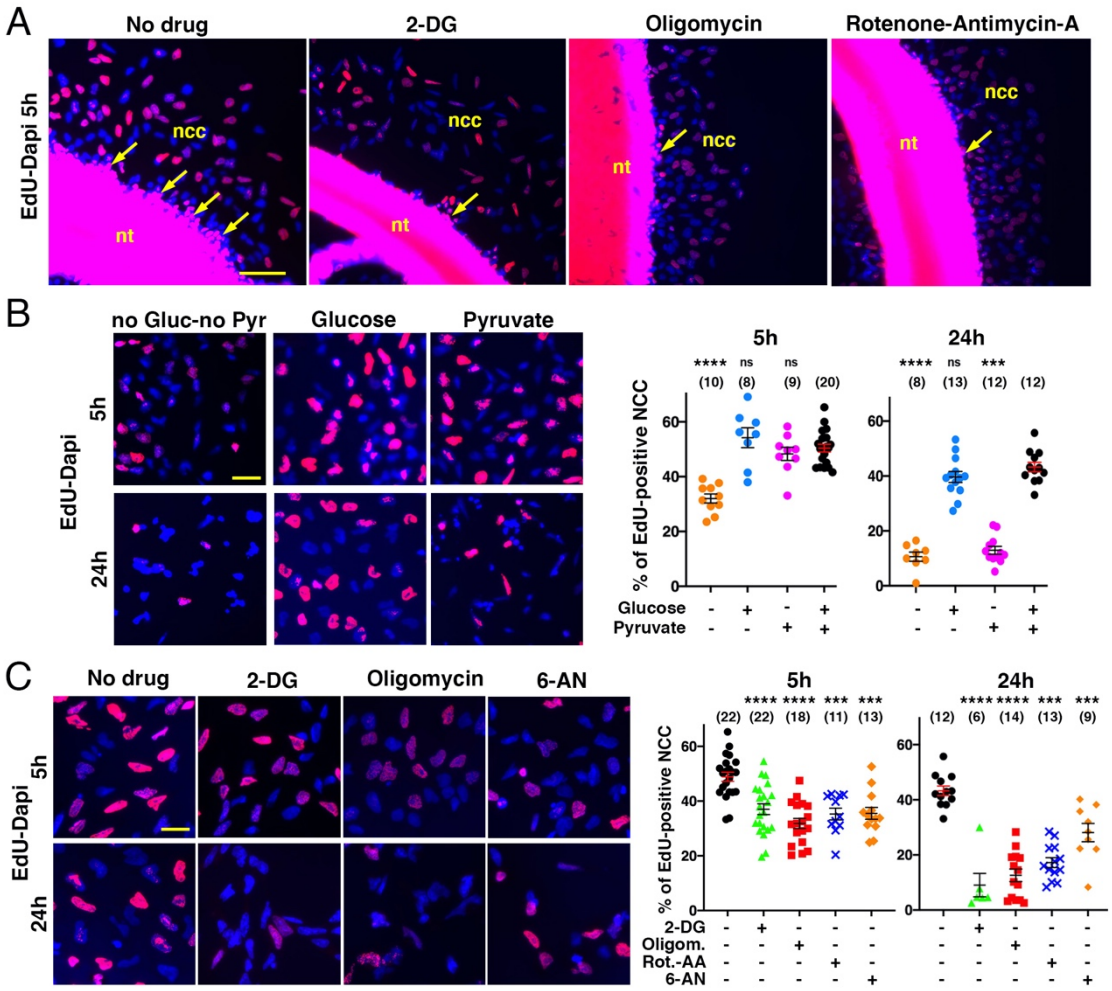

Supplementary Figure 7: Nekooie-Marnany et al.

163

Fig. S7.

(A) Images of EdU incorporation (pink) and visualization of nuclei using Dapi (blue) in NT explants cultured for 5 h in glucose and pyruvate medium with metabolic inhibitors. Arrows point on NCC delaminating out of the NT, which are EdU+, as some of the migrating NCC. (B, C) Images of EdU incorporation (pink) and visualization of nuclei using Dapi (blue) (left) and scatter plot with mean ± s.e.m of the proportion of EdU-positive NCC (right) in NT explants cultured for 5 h or 24 h in indicated nutrient condition (B) and in glucose and pyruvate medium with inhibitors (C). (n) indicate the number of NT explants analyzed. Scatter plots were analyzed using one-way ANOVA followed by Dunnett's multiple comparison test relative to the condition without the drug. Data were collected from at least three independent experiments. Images are from representative experiments. *** $P<0.001$, **** $P<0.0001$; ns, not statistically significant, $P>0.05$. Scale bar in A, 50 μm; and in B, C, 20 μm.

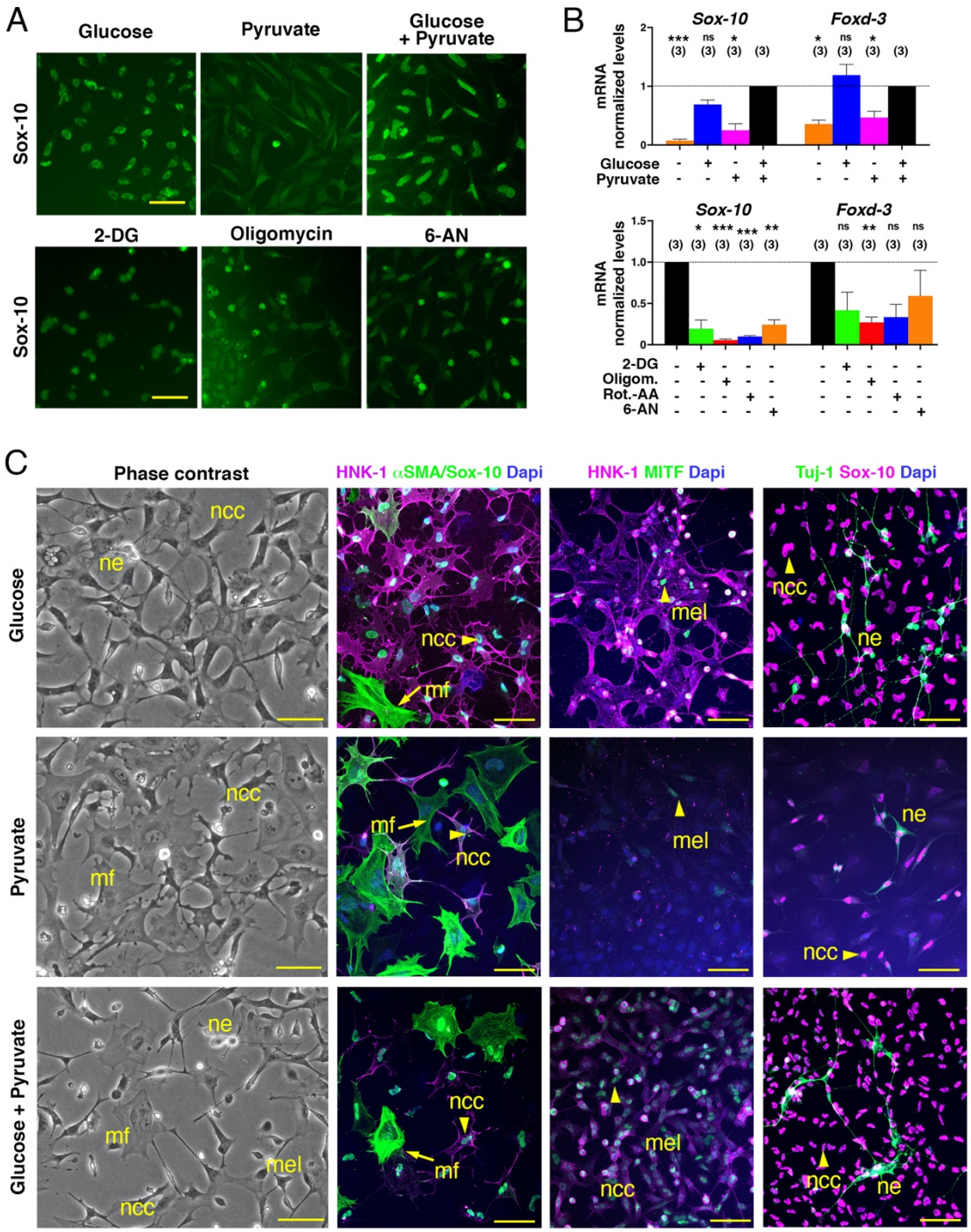

Supplementary Figure 8: Nekooie-Marnany et al.

177

Fig. S8, related to Fig. 6.

(A) Immunostaining for Sox-10 in NCC from trunk NT explants cultured for 24 h in indicated nutrient conditions (top) and with metabolic inhibitors (bottom). (B) Normalized levels of *Sox-10* and *Foxd-3* mRNA measured by qRT-PCR from NT explants cultured for 24 h in indicated nutrient conditions (top), and in glucose and pyruvate medium with metabolic inhibitors (bottom), with three. Values are mean ± s.e.m of triplicates per medium condition and gene analyzed using unpaired t-test two-tailed. (n) indicate the number of experiments. * $P<0.05$, ** $P<0.01$, *** $P<0.001$; ns, not significant, $P>0.05$. (C) Phase contrast and immunofluorescence images for pluripotency and differentiation markers, with nuclei labelled with Dapi (blue) showing the morphology and heterogeneity of the NCC population after 3 days in culture in medium containing glucose (top), pyruvate (middle) or both nutrients (bottom). Nuclear Sox-10 and HNK-1 mark undifferentiated NCC progenitors (arrowhead), α-SMA myofibroblasts (mf, arrows; left panels), nuclear MITF melanoblasts (mel, arrows, also negative for HNK1; middle panels), and Tuj-1 neurons (ne, in green right panels) with elongated neurites. Data were collected from at least three independent experiments. Images in A and C are from representative experiments. Scale Bars, 50 μm.